Low-Earth Orbit Flight Test of an Inflatable Decelerator Modeling and Reconstruction

Rohan G. Deshmukh*, Soumyo Dutta† Ashley M. Korzun‡ John M. DiNonno§ F. Mcneil Cheatwood¶
NASA Langley Research Center, Hampton, VA, 23666, USA

Christopher D. Karlgaard‖
Analytical Mechanics Associates, Inc., Hampton, VA, 23666, USA

Anthony L. Fine**
Cornell University, Ithaca, NY, 14853

The Low-Earth Orbit Flight Test of an Inflatable Decelerator (LOFTID) mission was a flight test performed on November 10, 2022. LOFTID is an 6 meter diameter Hypersonic Inflatable Aerodynamic Decelerator (HIAD) that is stowed for launch as a secondary payload, inflated in space, and separated from launch vehicle before conducting entry, descent, and landing (EDL). The main objective of the flight test was to demonstrate EDL at scale using HIAD technology at flight conditions relevant for future Earth and Mars missions. LOFTID successfully inflated and separated with a spin rate of 18 deg/s, landed within 1 hour on-parachute off the coast of Hawaii, and was successfully recovered. LOFTID re-entered Earth's atmosphere at 8 km/s, achieved peak deceleration of 9 Gs and peak heat rate of 40 W/cm^2, and demonstrated angle-of-attack stability throughout entirety of flight. On-board instrumentation provided flight data, which was saved onto an ejectable data recorder that was ejected at 18 km and successfully recovered. Despite the loss of inertial measurement unit data, techniques were developed to reconstruct the estimated flight performance as described in this paper. This paper presents the trajectory analysis, aerodynamics modeling, and reconstructed flight performance of the LOFTID re-entry vehicle.

Nomenclature

Presented as Paper 2024-1501 at the 2024 AIAA SciTech Forum, Orlando, FL, January 8–12, 2024
*Aerospace Engineer, Atmospheric Flight and Entry Systems Branch, AIAA Member
†Aerospace Engineer, Atmospheric Flight and Entry Systems Branch, AIAA Associate Fellow
‡Aerospace Engineer, Atmospheric Flight and Entry Systems Branch, AIAA Associate Fellow.
§LOFTID Chief Engineer, AIAA Member
¶LOFTID Principal Investigator, AIAA Senior Member
‖Aerospace Engineer, Atmospheric Flight and Entry Systems Branch, AIAA Associate Fellow.
**Undergraduate Student, Department of Engineering Physics.

C_A	axial force coefficient	Θ	Pitch angle, deg
C_l	rolling moment coefficient	θ	Azimuth, deg
C_m	pitching moment coefficient	σ	Standard deviation
$C_{m_{\dot{\alpha}}}$	aerodynamic pitching-moment slope coefficient	Φ	Roll angle, deg
C_{m_q}	aerodynamic pitch damping coefficient	ϕ	Aerodynamic roll angle, deg
C_N	normal force coefficient	φ	Co-latitude, deg
C_n	yawing moment coefficient	Ψ	Yaw angle, deg
C_{n_r}	yaw damping coefficient		
C_Y	side force coefficient	*Superscripts and Subscripts*	
D	capsule diameter, m	A	adder
Kn	Knudsen number	e	Earth
M	Mach number	C	coefficient
q	Dynamic pressure, Pa	CG	center of gravity
U	Uncertainty	$disp$	dispersed quantity
V	atmosphere-relative velocity, m/s	M	multiplier
X,Y,Z	capsule coordinates from nose, m	m	Moon
α	Angle of attack, deg	T	total condition
α_T	Total angle of attack, deg	∞	freestream condition
β	Angle of sideslip, deg		
γ	Inertial flight path angle, deg		

I. Introduction

The Low-Earth Orbit Flight Test of an Inflatable Decelerator (LOFTID) mission was the culmination of two decades of research and development for Hypersonic Inflatable Aerodynamic Decelerator (HIAD) technology by NASA. On November 10th, 2022, LOFTID launched from Vandenberg Space Force Base as a secondary payload ride-share with the National Oceanic and Atmospheric Administration's (NOAA) Joint Polar Satellite System 2 (JPSS-2) mission on a United Launch Alliance (ULA) Atlas V launch vehicle. After JPSS-2 was delivered to orbit, an inflated and spin-stabilized LOFTID separated from the Atlas V Centaur upper stage on a re-entry trajectory. LOFTID entered Earth's atmosphere at approximately 18,000 miles per hour and successfully survived entry, descent, and landing (EDL), splashing down in the Pacific Ocean 375 miles east off the coast of Hawaii. This work presents the pre-launch trajectory analysis and reconstructed flight performance of the LOFTID re-entry vehicle. This paper is organized as follows. Section I provides background on the origins of LOFTID through the development of HIAD technology.

Section II provides an overview of the trajectory modeling and simulation, including flight mechanics simulation, tools, and pre-launch trajectory analysis. Section III highlights the aerodynamics database development, including vehicle geometry modeling, static and dynamic aerodynamics, and aerodynamic uncertainty modeling. Section IV presents the day-of-launch results and post-flight reconstruction results, including overview of reconstruction data sources and best estimated trajectory reconstruction. Section V summarizes lessons learned and conclusions from the LOFTID flight demonstration mission.

A. Mission Summary

The objective of LOFTID was to develop, scale, and demonstrate entry performance of a flight-relevant HIAD to advance and mature the technology for future entry systems applications at Earth and other planetary bodies with atmospheres. With the ability to pack into a small volume for launch and to then deploy and inflate to a much larger diameter prior to atmosphere entry, HIAD is an enabling heatshield technology for decelerating heavy payloads at destinations with atmospheres. Traditional rigid aeroshells are constrained by the launch vehicle's payload fairing diameter. This limits the available aerodynamic drag area during entry, which ultimately constrains the mass of the payload to be delivered. For secondary payloads, the ability to stow into a compact form-factor and then deploy to a larger aeroshell diameter makes HIAD a compelling technology for NASA planetary missions as well as cost-effective payload returns at Earth. The LOFTID mission was required to produce the equivalent hypersonic aerodynamic drag of a rigid aeroshell of the same geometry and to maintain a total angle of attack less than 20 deg from entry through Mach 0.7 conditions (stable flight).

LOFTID was instrumented to provide large amounts of flight data in a relevant environment suitable for future Mars and Earth missions. A Flush Air Data Sensing System was engineered to provide in-situ pressure measurements throughout atmospheric flight. An Inertial Measurement Unit was utilized to provide measurements of LOFTID accelerations and rates during flight. Global Positioning System data from a locator beacon on LOFTID was utilized to provide live telemetry data of portion of the flown trajectory. Several video cameras were installed around the heatshield for providing flight footage. The combination of these data sources can allow for a reconstruction of the as-flown trajectory to quantify performance relative to mission objectives.

B. HIAD History

LOFTID was designed as a 6 meter diameter aeroshell for entry from low-Earth orbit, which makes LOFTID the largest blunt body aeroshell flown to-date. The selection of the diameter was a result of balancing the largest scale achievable within the mass and volume constraints for a secondary payload against a suitable ballistic coefficient to achieve similar aeroheating to Mars HIAD entry mission concepts [1]. LOFTID's 70 deg sphere-cone geometry was constructed from an inflatable structure and flexible thermal protection system, which when fully deployed and inflated,

functioned as both a decelerator and heatshield. The flight test is a significant next step for HIAD technology, building on the successes of the Inflatable Reentry Vehicle Experiment (IRVE II[2] and IRVE-3[3]) missions, which were 3 meter diameter aeroshells deployed from suborbital sounding rockets.

The next section highlights the trajectory modeling and simulation efforts that were developed for the LOFTID flight test.

II. Trajectory Modeling and Simulation

Figure 1 shows the concept of operations for LOFTID. Following launch into low-Earth orbit and separation of the primary payload, the LOFTID aeroshell, or Re-entry Vehicle (RV), was inflated, oriented for entry, spun up to 18 deg/s, and separated from the Centaur upper stage of the launch vehicle. Entry interface was defined at 125 km altitude. The RV rapidly decelerated through key EDL events, such as peak deceleration and heating (described later in Section II.A). Upon decelerating to subsonic speeds, the ejectable data recorder (EDR) and parachute deployment occurred with both events set on time triggers. The mission officially ended when the RV reached Mach 0.7, and the EDR was jettisoned for recovery. Deceleration of the RV continued through subsonic conditions with the eventual deployment of a parachute and splashdown. While not a mission requirement, it was highly desirable to recover the RV. The RV was not fully designed to remain buoyant, in the case of water submerging the backside of the heatshield. Consequently, the EDR contained a copy of all flight measurements and was designed to remain bouyant post-splashdown. As explained in this document, both the EDR and the RV were successfully recovered from the ocean post-flight. The trajectory modeling and simulation of LOFTID was focused on EDL, starting from RV separation and ending at splashdown.

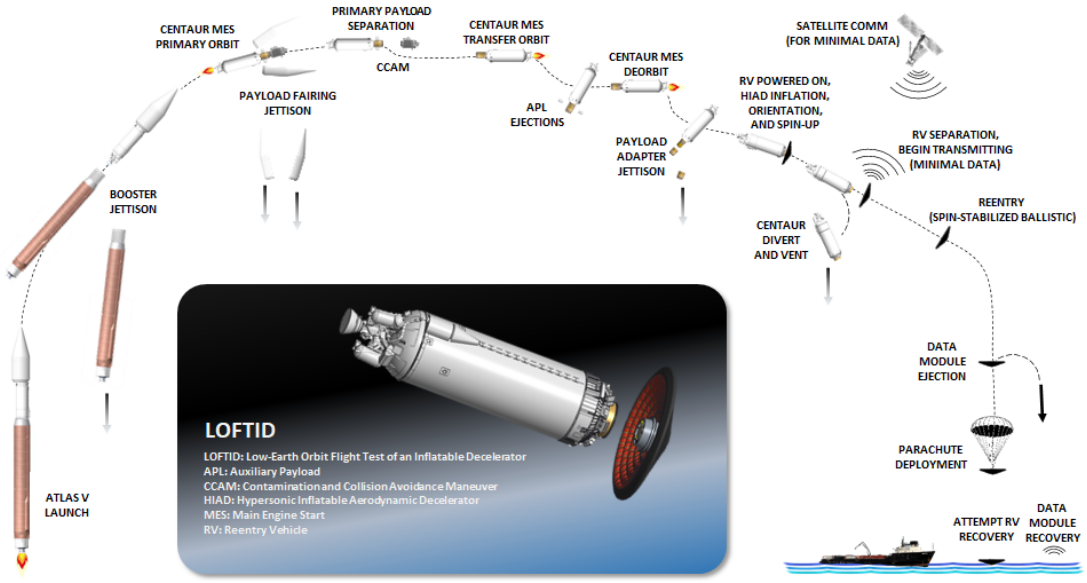

Fig. 1 LOFTID Concept of Operations.

A. Flight Mechanics Simulation

Flight mechanics analysis for LOFTID was conducted using the Program to Optimize Simulated Trajectories II (POST2) [4, 5]. POST2 is a system-of-systems software that allows for the ingestion of subsystem models to simulate the overall 6 degree-of-freedom (DOF) EDL trajectory. The framework for the POST2 implementation of LOFTID is shown in Figure 2. Many of the subsystem models were developed in-house at NASA Langley Research Center (LaRC), including the EDR, aerothermodynamic database, aeroshell mass properties, and aerodynamics database. The EDR is modeled as a secondary vehicle in the POST2 simulation that separates from the RV using a spring-eject mechanism[6]. The EDR ballistic trajectory post-ejection is simulated down to splashdown and analyzed for recovery planning. The aerodynamics database is discussed in more detail in Section III. The aerothermodynamic database consisted of indicator values applied at different points on the forebody aeroshell. The indicators are empirical curve-fit equations to computational fluid dynamics (CFD) data, which provide the POST2 trajectory a prediction of the aeroheating environment. More information on the aerothermodynamic database can be found in Reference [7]. Aeroshell mass properties is modeled using predicted day-of-launch values with model uncertainties. The atmosphere models utilized include EarthGRAM 2010 [8], developed at NASA Marshall Space Flight Center (MSFC), and atmosphere profiles generated by the Goddard Earth Observing System Model Version 5 (GEOS-5), which is operated by NASA Goddard Space Flight Center's (GSFC) Global Modeling and Assimilation Office (GMAO) [9, 10]. EarthGRAM is a general engineering model that utilizes climatological data to define atmospheric properties, but it is not a forecast model that predicts the atmospheric properties on a certain day. On the other hand, GEOS-5 are weather forecast models. More information on these two atmosphere models can be found in Section IV.B.1. The parachute system model was developed by Airborne Systems. The portion of the overall test timeline analyzed using POST2 occurs from RV separation to LOFTID splashdown. For simulation initialization at separation, two methods were developed. The first method, utilized during pre-launch, included initial state and separation attitude data provided by the NASA Kennedy Space Center (KSC) Launch Service Provider and ULA, respectively. The second method, utilized during operations, included an orbital parameter message (OPM) update file provided by ULA. The OPM contained information on the LOFTID trajectory position/velocity and RV attitude angles/rates at separation.

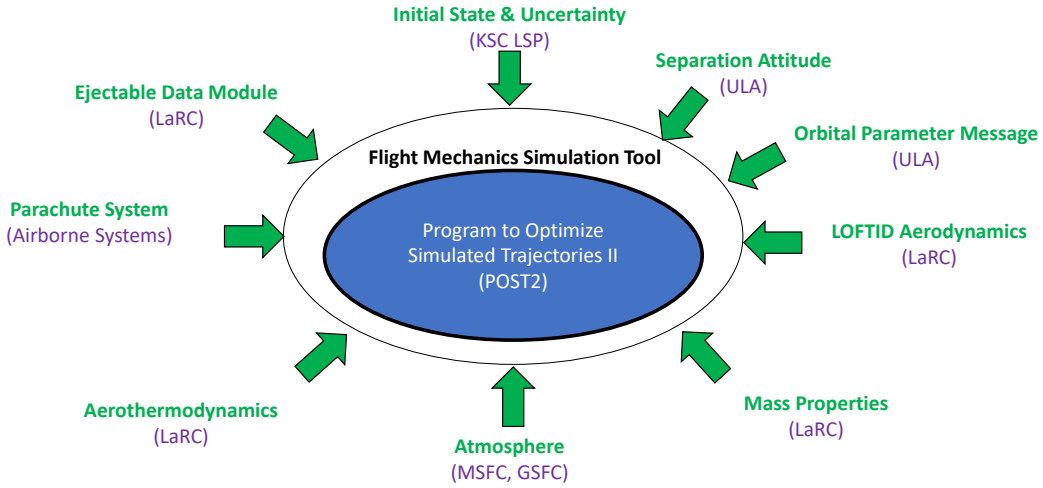

Fig. 2 LOFTID Flight Mechanics Simulation Tool.

B. Simulation Automation

Similar to past projects that have needed fast turnaround of trajectory analyses [11, 12], LOFTID used an automation program called Jenkins to script the execution of trajectory analysis. This analysis included automation of Monte Carlo runs using the OPM during flight operations and automation of daily pre-flight prediction runs using 72-, 48-, and 24-hour GEOS-5 weather forecasts. The automation and scripting reduces the chances of human error, such as inputting the wrong setting, and allowed the analyst to concentrate on the results to see if it was useful for recovery operations.

C. Pre-Launch Trajectory Analysis

Prior to launch, a trajectory simulation campaign was conducted based on the ULA-provided best estimated trajectories. The launch window, from open to close, for Atlas V was 36 minutes long. LOFTID EDL trajectory analysis was conducted for three time periods within the launch window (open -> Minus 18 min from center of launch window, middle -> Plus 0 min from center of launch window, and close -> Plus 18 min from center of launch window) using ULA-provided Centaur separation state data. The flight mechanics error modeling used in the Monte Carlo analysis can be found in Reference [13].

8001 Monte Carlo simulations were run for the open, middle, and close launch windows. Table 1 and Table 2 provides a summary of the key EDL trajectory metrics. Statistics are reported to the $\pm 2\sigma$ confidence interval. The main effect the launch window has on the LOFTID EDL trajectory is on the separation state. The time propagated from LOFTID RV separation to entry interface at 125 km altitude is shown to vary. Open and close of the launch window have similar times, whereas the middle launch window is approximately 50 sec longer. The entry velocities, entry total

angles of attack, and entry flight path angles are comparable over the launch window. Trajectory performance metrics such as peak deceleration, peak dynamic pressure, max heat rate at nose, and max heat load at nose are also comparable over the window. The only noticeable sensitivity caused by the longer time-of-flight is time-based events. Given that the LOFTID EDR and pilot chute triggers are timer-based (2260 sec since RV separation for EDR trigger and 2509 sec since RV separation for pilot chute trigger), the increase in time-of-flight leads to these two triggers occurring at higher altitudes and Mach numbers. The pilot chute trigger deploys at an average total angle of attack of less than 5 deg over the entire launch window. It provides sufficient vertical deceleration for splashdown of less than 15 mph. The non-zero horizontal splashdown speeds are driven by horizontal winds. Figure 3 shows 2σ splashdown ellipses with ellipse major and minor axes along with the latitude/longitude of the ellipse center produced over the open, middle, and close windows.

The information obtained from this pre-launch trajectory cycle was used to inform planning for LOFTID mission timeline and recovery. A timeline was developed to inform when key EDL events will occur during launch operations. Splashdown ellipses were used to inform the recovery boat on what region of the Pacific Ocean the LOFTID RV and EDR were expected to land. Going into launch, a series of improvements to the trajectory simulation architecture were developed. These included the utilization of atmosphere forecast data in lieu of November mean monthly atmosphere in EarthGRAM 2010 as well as integration of simulation automation into trajectory result generation process.

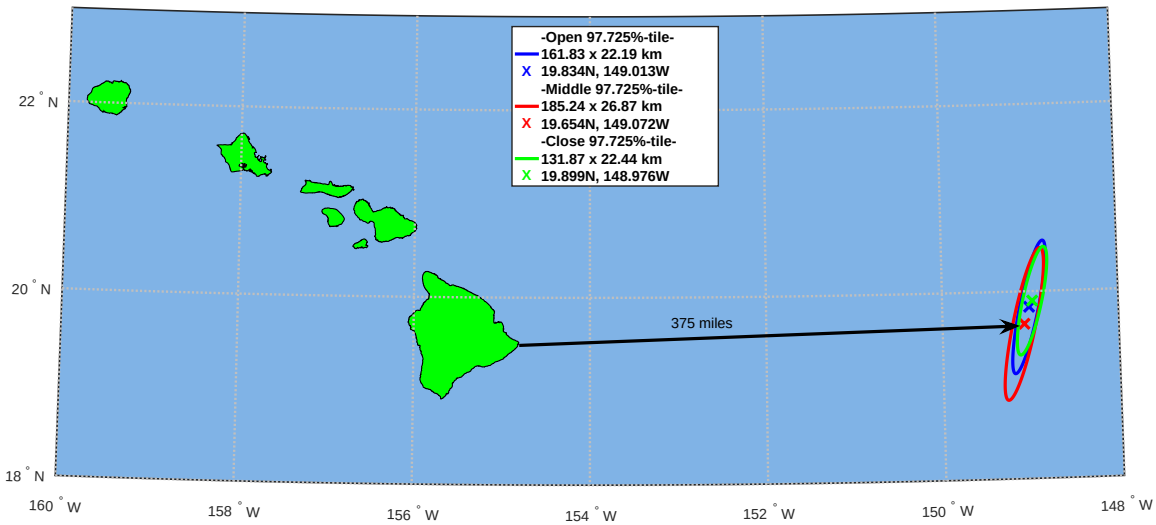

Fig. 3 Pre-Launch BET Analysis Splashdown Ellipses

Table 1 Pre-Launch LOFTID EDL Trajectory Analysis Results. Triad of data for each performance metric corresponds to open, middle, and close BET trajectories respectively.

	2.275%-tile	Mean	97.725%-tile
Time from RV Separation to Entry (s)	1804.88	1811.77	1818.90
	1851.79	1860.00	1867.04
	1810.29	1815.72	1821.21
Entry Flight Path Angle (deg)	-2.2969	-2.2845	-2.2714
	-2.2974	-2.2809	-2.2651
	-2.3027	-2.2899	-2.2770
Entry Velocity (km/s)	8.0212	8.0219	8.0226
	8.0204	8.0218	8.0230
	8.0214	8.0221	8.0228
Entry Total Angle of Attack (deg)	0.4654	3.0672	7.5490
	0.4514	3.1553	7.5985
	0.4434	2.9578	7.3822
Peak Deceleration (Earth g)	8.7872	9.6586	9.6597
	8.7659	9.5112	9.6221
	8.8029	9.6487	9.6751
Peak Dynamic Pressure (Pa)	2035.2842	2158.2550	2242.8670
	2028.6395	2130.0579	2234.9646
	2038.4477	2139.8698	2246.9269
Max Heat Rate at Nose (W/cm^2)	38.0537	39.2735	40.5231
	37.9843	39.1956	40.4554
	38.1141	39.3295	40.5942
Max Heat Load at Nose (kJ/cm^2)	3.4410	3.5222	3.6076
	3.4422	3.5245	3.6103
	3.4379	3.5186	3.6030

*Table continued on next page

Table 2 Continuation of Table 1

	2.275%-tile	Mean	97.725%-tile
Altitude at EDR Jettison (km)	14.5655	15.2421	15.9077
	17.8863	18.7503	19.5566
	14.8514	15.4586	16.0256
Mach Number at EDR Jettison	0.2073	0.2178	0.2312
	0.2761	0.2967	0.3178
	0.2130	0.2220	0.2350
Altitude at Pilot Chute Trigger (km)	3.4440	4.3394	5.0785
	5.2102	6.0492	6.7307
	3.5662	4.4461	5.1619
Total Angle of Attack at Pilot Chute Trigger (deg)	0.3392	4.7271	24.5274
	0.3567	4.6577	23.2903
	0.3503	4.7362	25.0208
Time from Entry to Splashdown (s)	1199.74	1364.85	1519.95
	1379.76	1544.94	1723.52
	1215.29	1376.85	1531.01
Horizontal Velocity at Splashdown (m/s)	2.5895	8.1665	13.8537
	2.6353	8.1377	13.8407
	2.6035	8.1690	13.8974
Vertical Velocity at Splashdown (m/s)	4.7575	5.6464	6.5653
	4.7344	5.6498	6.5677
	4.7539	5.6457	6.5481

III. Aerodynamics Database Development

Aerodynamic forces and moments are key contributors to entry vehicle performance, including drag and stability. This section describes the development and implementation of the aerodynamics database used to support design and pre-flight performance assessments for LOFTID.

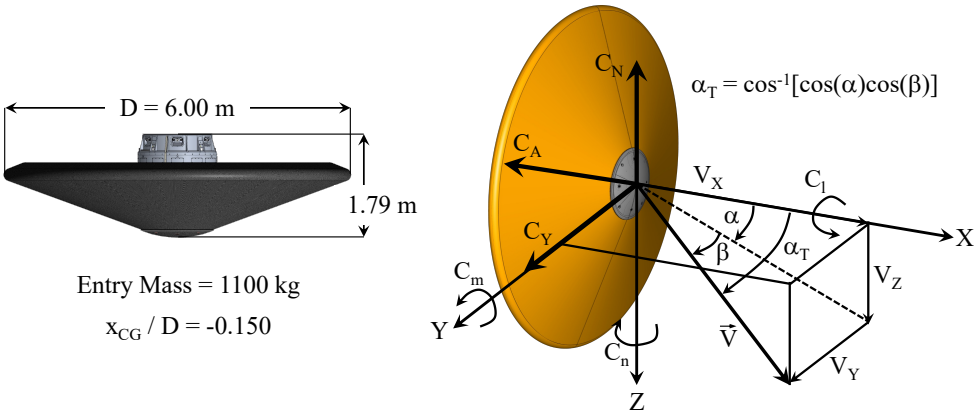

Fig. 4 LOFTID Geometry (left) and Aerodynamics Coordinate Frame (right).

Fig. 4 shows both the geometry and aerodynamics coordinate system of LOFTID, which is typical for blunt-body entry shapes. The geometry of the RV was modeled to be fully smooth, rigid, and axisymmetric for the purpose of aerodynamic analyses. To demonstrate satisfaction of mission requirements, the aerodynamics database was developed to cover the entire trajectory from atmospheric interface (125 km altitude) to splashdown and span the range of potential conditions and attitudes anticipated in flight across design maturation of the RV, atmosphere variability, and launch window impacts. The aerodynamics database (ADB) developed for LOFTID provides 6-DOF aerodynamic force and moment coefficients as a model input to the trajectory simulation as a function of flight conditions and vehicle attitude. The model spans non-continuum and continuum flight regimes, static aerodynamics and dynamic pitch damping, and uncertainties as a function of flight regime. Inputs to the aerodynamics database are freestream Knudsen number (Kn), Mach number (M_∞), angle of attack (α), and angle of sideslip (β). Aerodynamic force and moment coefficients are specified by total angle of attack (α_T), assuming the RV is axisymmetric. Logic is developed in the ADB to utilize input data for the appropriate flight regime (free-molecular, transitional, hypersonic, supersonic, transonic, and subsonic). Dispersion of aerodynamic coefficients for Monte Carlo trajectory analysis are also handled within the aerodynamics database, and details on the implementation are given in Section III.D.

A. Vehicle Geometry and Reference Trajectory

The aerodynamics datasets, methods, tools, and implementation draw strongly on heritage from IRVE [14], IRVE-3 [3], and other NASA entry capsule missions [15–17]. Different computational tools and methods are required for each flow regime to capture relevant physics, and these tools, methods, heritage, and applicability are briefly discussed in the

following sections, with further details provided in Ref. [7]. Figure 5 shows the design reference trajectory as a function of both altitude and velocity, with flow regimes noted and the static anchor points used in the interpolation within the aerodynamics database denoted along the reference trajectory. Individual conditions are simulated using more than one computational approach across the boundaries of each flow regime (indicated by the overlap conditions in Fig. 5b) and the data blended through the transition. The following sections describe the static aerodynamics, dynamic pitch damping, and uncertainties developed and applied for LOFTID.

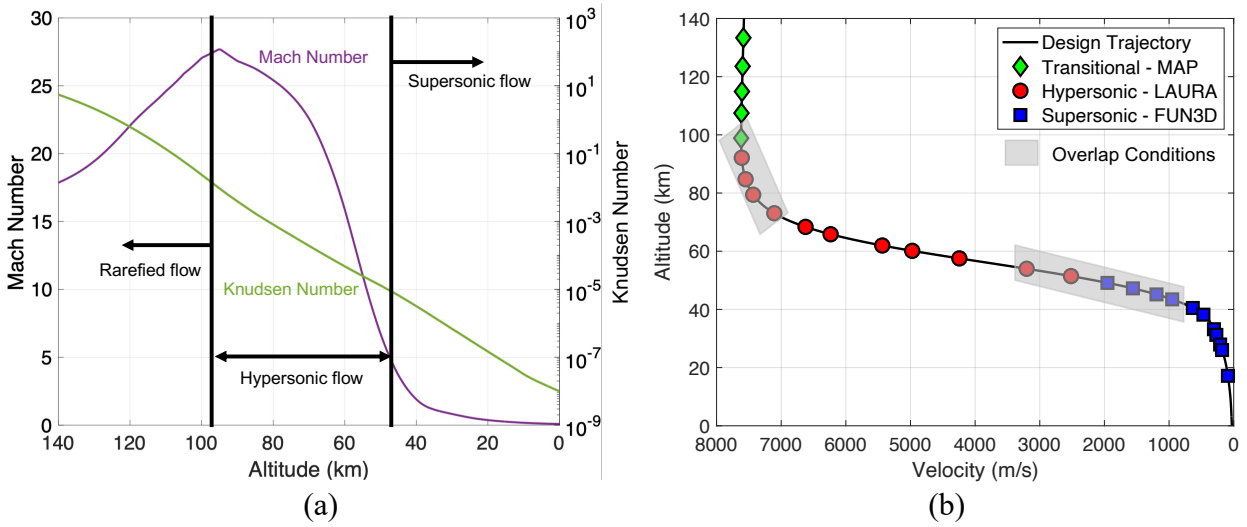

Fig. 5 LOFTID Reference Trajectory (a) and Aerodynamics Database Anchor Points (b).

B. Static Aerodynamics

The tools and methods applied to generate static aerodynamics data for LOFTID have been successfully applied to and validated by flight on Earth and Mars for blunt entry capsules with strong detached shocks and highly separated wake flows. Table 3 outlines the organization of the ADB by flight regime, including the range of conditions, input parameters, and data source. All static aerodynamics data for LOFTID are sourced from computational tools, sharing solutions generated for aerothermodynamics analysis [7]. The assumption that the vehicle is axisymmetric allows the aerodynamic coefficients to be defined in the α_T plane and then decomposed into the α and β planes for use in the 6-DOF trajectory simulation (see Fig. 4).

At the highest altitude conditions below the atmospheric interface (125 km), non-continuum aerodynamics require prediction using methods that account for molecular interactions between individual molecules and those molecules with the vehicle. Due to the similarity in general shape and high-altitude environment, free-molecular data originally generated for IRVE-3 [3] using the Direct Simulation Monte Carlo (DSMC) Analysis Code (DAC [18]) were used for conditions where $Kn > 3.018$ (above 133 km on the design reference trajectory) and tabulated for α_T from 0 deg to 180 deg. Transitional data were generated using the Multiphysics Algorithm with Particles (MAP)[19] DSMC code to

Table 3 LOFTID Static Aerodynamics Sources

	Flight Regime	Range (n.d., deg)	Input Parameters	Source
Non-Continuum	Free-Molecular	$Kn > 3.018$, $0 \leq \alpha_T \leq 180$	α_T	DAC [18]
	Transitional	$0.00572 \leq Kn \leq 3.018$, $0 \leq \alpha_T \leq 8$	α_T, Kn	MAP [19]
Continuum	Hypersonic	$M_\infty \geq 7.88$ and $Kn < 0.00572$, $0 \leq \alpha_T \leq 8$	α_T, M_∞	LAURA [20]
	Supersonic	$0.89 < M_\infty \leq 6.10$, $0 \leq \alpha_T \leq 20$	α_T, M_∞	FUN3D [21]
	Mid-Subsonic	$0.30 < M_\infty \leq 0.89$, $0 \leq \alpha_T \leq 40$	α_T, M_∞	FUN3D
	Low-Subsonic	$M_\infty \leq 0.30$, $0 \leq \alpha_T \leq 40$	α_T	FUN3D

populate additional low-density conditions down to Kn = 0.00572 (92 km), eliminating the need for a sine-squared bridging function and directly connecting the free-molecular and continuum flow regimes [7]. The transitional flow data were generated for α_T from 0 deg to 8 deg, with the α_T range guided by permissible RV separation conditions and the ballistic trajectory design. These flow solutions employed reacting gas chemistry with surface catalysis and Cartesian/cut-cell grid topologies; the top section of Fig. 6 shows an example MAP solution for LOFTID at a non-zero angle of attack. Hypersonic continuum data were generated using the Langley Aerothermodynamic Upwind Relaxation Algorithm (LAURA) Navier-Stokes flow solver [7, 20, 22] with non-equilibrium chemistry and structured grid topologies. The middle of Fig. 6 shows an example LAURA mesh and flow solution, with forebody-only data used within the ADB for this flight regime. Hypersonic continuum data in the ADB span Mach numbers from 27.2 to 6.1 and total angles of attack from 0 deg to 8 deg, with the α_T range intended to bound any potential excursions from the ballistic trajectory design due to small unintended changes in shape or mass properties.

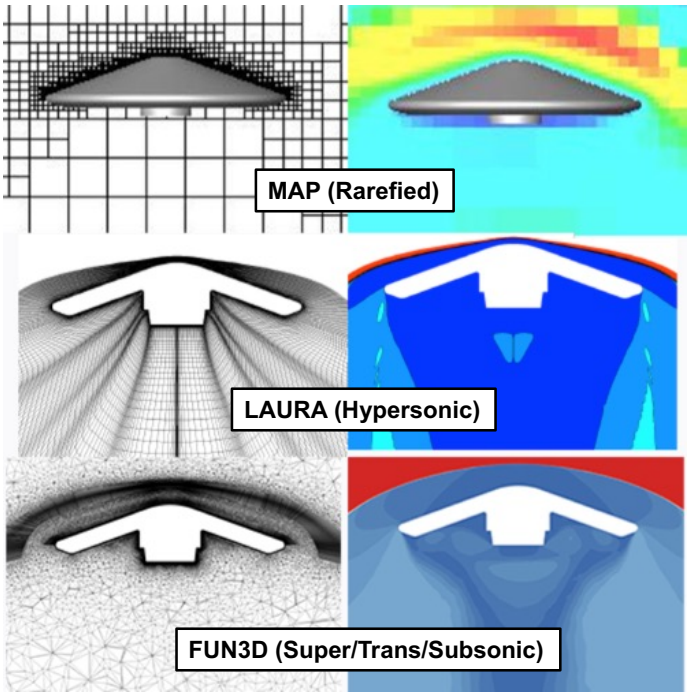

Fig. 6 Examples of Mesh and Flow Solutions for Computationally Modeled Static Aerodynamics Data.

The remaining static aerodynamics along the design reference trajectory were generated using the Fully Unstructured Navier-Stokes 3-Dimensional (FUN3D)flow solver [7, 21], with an example mesh and solution shown at the bottom of Fig. 6. For supersonic, transonic, and subsonic conditions, data were generated for Mach numbers from 6.1 down to 0.3 and a wider range of α_T (0 deg to 40 deg) to avoid potential extrapolation through conditions where blunt body geometries characteristically exhibit attitude growth due to inherent dynamic instability at low supersonic Mach numbers. Supersonic static coefficients in many prior ADBs [15–17, 23] used forebody CFD solutions with a Viking-derived pressure correction for aftbody contributions [16, 23], but these shapes all have full backshells protruding into the wake. For supersonic and subsonic conditions, IRVE and IRVE-3 used static coefficients derived from ballistic range testing [2, 3], as the aft configurations, like LOFTID, lacked a backshell and instead had a predominantly concave geometry with a slender, protruding payload along the center axis. LOFTID used time-averaged, unsteady Navier-Stokes three-dimensional flow solutions from FUN3D, including the aft payload geometry and wake, perfect-gas air assumptions, and fully unstructured grids, for all conditions in the ADB from Mach 6.1 to 0.3. These data were used for the RV while descending by parachute through to splashdown, with static aerodynamics coefficients for all conditions below Mach 0.3 held constant at the Mach 0.3 values, though still a function of α_T.

Figures 7, 8, and 9 show the nominal static aerodynamics for axial force coefficient and pitching moment coefficient, where C_m is shown about the center-of-gravity (CG) location 0.150 diameters aft of the nose. Axial force dominates the aerodynamic forces on blunt body vehicles ($C_A >> C_N$). As the vehicle decelerates from the top of the atmosphere, C_A

continuously decreases from rarefied to continuum conditions. C_A is greatest at the lowest angles of attack, consistent with the forebody surfaces being by far the most significant contributor to the pressure load on the vehicle. C_A continues to gradually decrease as the vehicle decelerates further, until reaching low-supersonic conditions. Beginning near Mach 3.0, C_A rises with decreasing Mach number, as the pressure on the aft surfaces of the vehicle contributes a non-negligible pressure increment to the overall axial force. The aft pressure effects are less sensitive to angle of attack, and as the vehicle decelerates further, the strong pressure recovery across the shock disappears, and C_A quickly falls to a minimum. For conditions below Mach 0.3, C_A is held constant at the incompressible Mach 0.3 value and is then only a function of α_T.

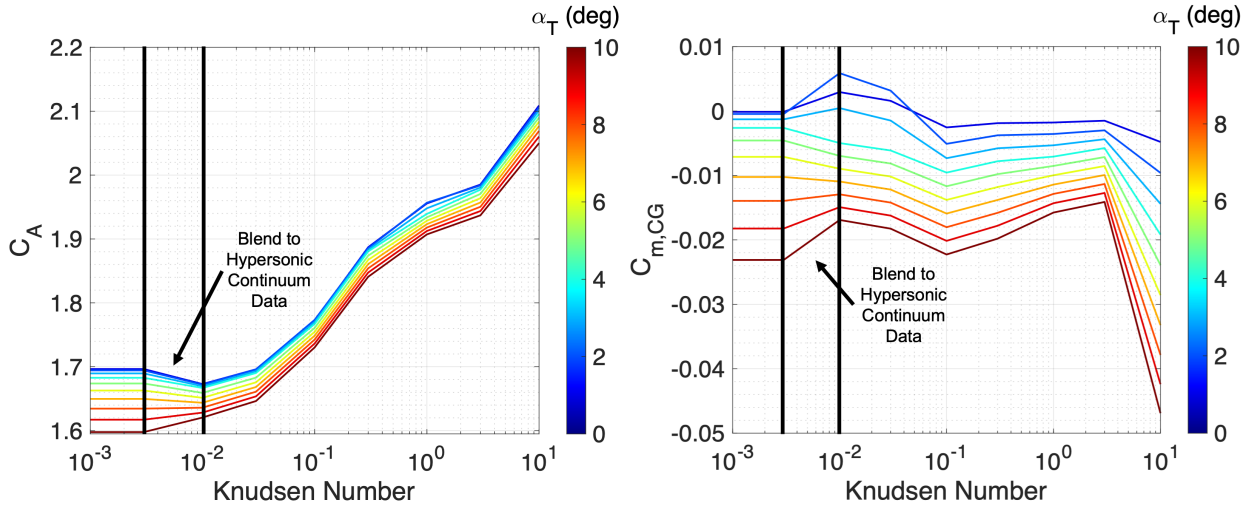

Fig. 7 LOFTID Non-Continuum Static Aerodynamics for Axial Force Coefficient (left) and Pitching Moment Coefficient (right).

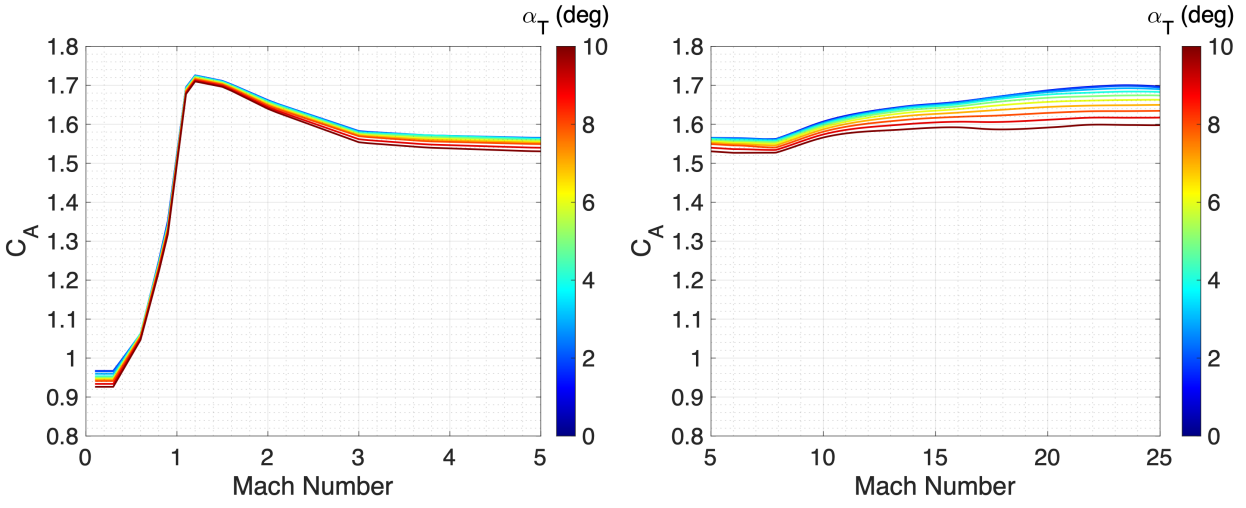

Fig. 8 LOFTID Continuum Axial Force Coefficient Database.

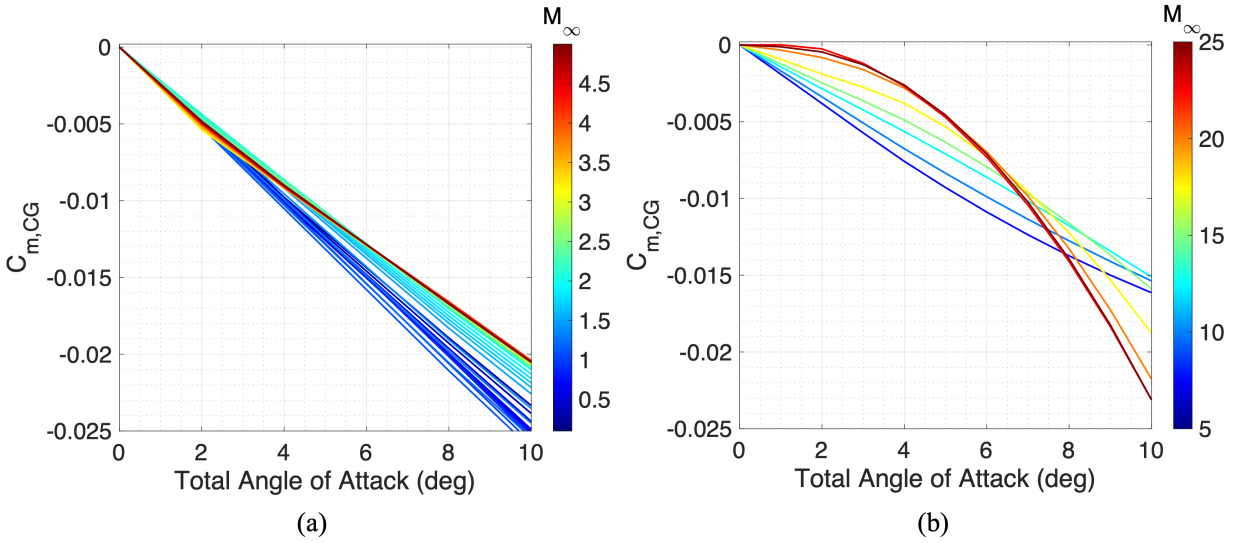

Fig. 9 LOFTID Continuum Pitching Moment Coefficient Database for (a) $M_\infty \leq 5$ and (b) $5 \leq M_\infty \leq 25$.

Figure 9 shows the pitching moment coefficient database for continuum conditions, with C_m plotted about the CG as a function of α_T and M_∞. The vehicle was predicted to be statically stable throughout the continuum conditions along the entry trajectory, as indicated by the persistent negative slope of $C_{m,CG}$ vs. α in Fig. 9. While Fig. 7 shows a small static instability at very low α_T (less than 2 deg) for $0.01 < Kn < 0.1$, the dynamic pressure at these conditions, due to the very low density at high altitude, produces a near-negligible effect on RV stability.

C. Dynamic Pitch Damping

Blunt body shapes are characteristically dynamically unstable at supersonic speeds [24], with undamped pitch oscillations corresponding to vehicle attitude and attitude rate growth as the vehicle decelerates through supersonic to transonic conditions. These effects have the potential to produce unfavorable dynamics, and for LOFTID, there was a stability requirement for the total angle of attack to not exceed 20 deg down to Mach 0.7. This allowed for successful deployment of the ejectable data module and later deployment of a subsonic parachute to limit the vertical speed at splashdown to below 6.7 m/s (15 mph). LOFTID deployed a parachute at low subsonic conditions to reduce vertical speed for splashdown, long past where the shape's inherent pitch damping instability is a dominant factor in the vehicle's dynamics.

Table 4 dows the LOFTID dynamic pitch damping sources and Figure 10 shows the dynamic damping database. The pitch damping coefficient model is a functional form based on instantaneous angle of attack and Mach number and is derived from ballistic range testing conducted for IRVE-3 [3]. The variable C_{m_q} here is the sum $C_{m_q} + C_{m_{\dot{\alpha}}}$, truncated for brevity. For free-molecular conditions, the vehicle is assumed to be dynamically stable at a fixed value of C_{m_q} = -0.32, consistent with assumptions made for IRVE-3 and validated through flight observation. For continuum conditions

above Mach 6, the vehicle is dynamically stable ($C_{m_q} < 0$), with C_{m_q} fixed at a value estimated from Newtonian flow approximations. Between free-molecular and hypersonic continuum conditions, the value of C_{m_q} is computed as a function of Kn using a sine-squared bridging function, the functional form commonly used for bridging blunt body aerodynamics [25]. The vehicle is dynamically unstable ($C_{m_q} > 0$), for $M_\infty < 3.5$ at very small angles of attack. For $M_\infty < 2.0$, the vehicle is dynamically unstable, but for a slightly larger range of angle of attack, up to 5 deg. For $M_\infty < 0.65$, C_{m_q} is held constant at the $M_\infty = 0.65$ value. The end of experiment for LOFTID is Mach 0.7, and blunt body dynamics are largely damped once the vehicle has decelerated through transonic conditions.

Table 4 LOFTID Dynamic Pitch Damping Sources

	Flight Regime	Range (n.d., deg)	Input Parameters	Source
Non-Continuum	Free-Molecular	$Kn \geq 10.0$, $0 \leq \alpha_T \leq 180$	none	–
	Transitional	$0.001 < Kn < 10.0$, $0 < \alpha_T < 40$	α_T, Kn	–
Continuum	Hypersonic	$M_\infty \geq 6.0$ and $Kn < 0.001$, $0 \leq \alpha_T \leq 40$	α_T, M_∞	IRVE-3
	Supersonic	$0.65 \leq M_\infty < 3.0$, $0 \leq \alpha_T \leq 40$	α_T, M_∞	IRVE-3
	Subsonic	$M_\infty < 0.65$, $0 \leq \alpha_T \leq 40$	α_T, M_∞	IRVE-3

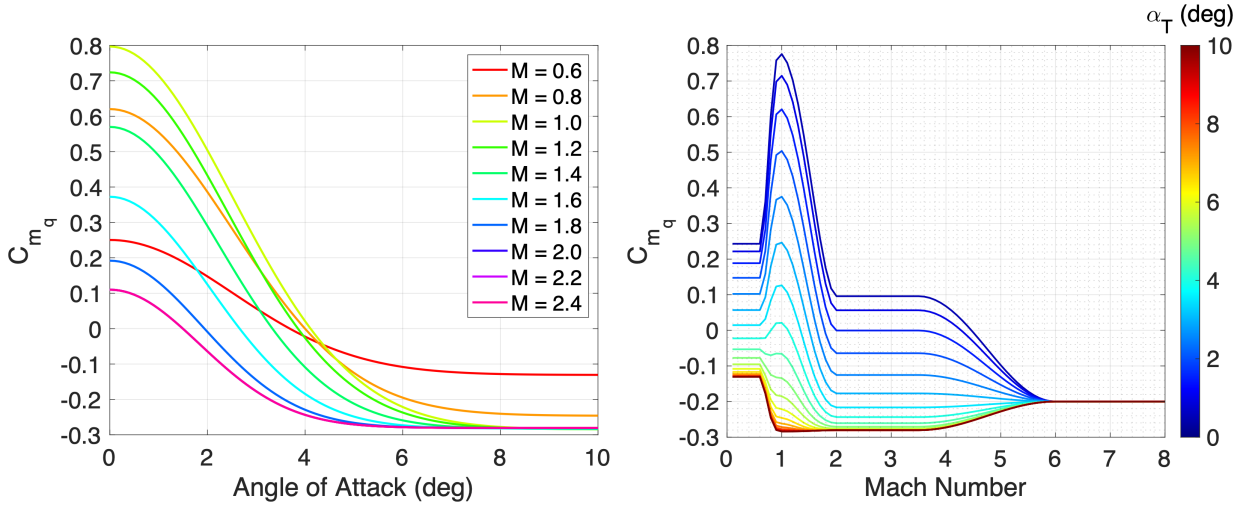

Fig. 10 LOFTID Dynamic Damping Database.

D. Aerodynamics Uncertainties

Pre-flight performance for LOFTID was assessed using Monte Carlo simulations with 6-DOF trajectories in POST2[13]. Uncertainties on the nominal aerodynamics data were defined as functions of flow regime within the ADB to allow for dispersion of aerodynamics within the analyses, with significant heritage from past flight experience and engineering judgement from IRVE, IRVE-3, Genesis, and Phoenix. Table 5 lists the aerodynamics uncertainties applied for LOFTID. Similar to the structure of the ADB for nominal aerodynamics, the uncertainties were defined by relevant flow regime. The differences in uncertainty magnitudes in Table 5 reflect differences in applicability, fidelity, and

uncertainty in the underlying tools, methods, and sources used to generate the nominal aerodynamic coefficients. For all static coefficients other than C_A and C_l, uncertainty adders and multipliers were applied to independently disperse trim attitude (intercept) and static stability (slope), respectively. C_A and C_l have adders only. Eq. 1 specifies the implementation of the static aerodynamics adders and multipliers given in Table 5, where the multipliers are indicated by a percentage. Uncertainties were applied after the ADB coefficients have been decomposed into the vehicle body frame (see Fig. 4), and all moments were dispersed about the CG, not the moment reference point (center of the heatshield).

Table 5 LOFTID aerodynamics uncertainties

Static Aerodynamics (Uncorrelated)				
Flight Regime	C_A	C_N, C_Y	C_m, C_n	C_l
Free-Molecular / Transitional $Kn > 0.1$	±5%	±0.01, ±20%	±0.005, ±20%	$\pm 1.24 \times 10^{-6}$
Hypersonic $M_\infty < 10$	±3%	±0.01, ±20%	±0.003, ±20%	$\pm 1.24 \times 10^{-6}$
Supersonic $1.5 < M_\infty < 5$	±10%	±0.01, ±20%	±0.005, ±20%	$\pm 1.24 \times 10^{-6}$
Transonic $0.4 < M_\infty < 1.5$	±10%	1.25 × Supersonic	1.25 × Supersonic	$\pm 1.24 \times 10^{-6}$
Dynamic Damping (Correlated)				
Flight Regime	C_{m_q}	C_{n_r}		
Transitional / Free-Molecular $Kn > 0.1$	±0.15	±0.15		
Hypersonic $M_\infty > 6$	±0.15	±0.15		
Supersonic $1.5 < M_\infty < 3$	+0.4 × [1.5, 0.5] − 0.4 + [0.1, 0.0]	+0.4 × [1.5, 0.5] − 0.4 + [0.1, 0.0]		
Transonic $1 < M_\infty < 1.5$	1.25 × Supersonic	1.25 × Supersonic		

All static aerodynamics uncertainties were uncorrelated and dispersed using a normal distribution, with the exception of C_l, which was dispersed using a uniform distribution. Increases in the multipliers for C_Y and C_N were applied over the IRVE-3 uncertainties as a result of potential limited deflection of the inflatable aeroshell under load. The uncertainty in C_{m_q} was fixed to be equal to that in C_{n_r}, and the implementation is specified in Eq. 2. For dynamic aerodynamics uncertainties, at hypersonic conditions, uncertainties were applied assuming a uniform distribution, and at supersonic and transonic conditions, the uncertainty adder was applied assuming a uniform distribution, and the uncertainty multiplier was applied assuming a normal distribution. An additional shift was applied to force a larger portion of the Monte Carlo cases to be less dynamically stable. The shift magnitude of 0.4 for $M_\infty < 3.0$ bounded the

ballistic range data underpinning the dynamic pitch damping model.

$$C_{disp} = [C_{nominal}(\alpha, \beta) + U_C^A](1 + U_C^M) \tag{1}$$

$$C_{m_q,disp} = (C_{m_q,nominal}(\alpha, \beta) - 0.4) * U_C^M + 0.4 + U_C^A \tag{2}$$

IV. Post-Flight Trajectory Reconstruction

Section II and Section III highlighted the flight mechanics simulation and aerodynamics database that were both utilized for LOFTID pre-launch analysis. This section discusses both the day-of-launch-performance and the reconstruction of the as-flown trajectory. In this section, certain data sources utilize Coordinated Universal Time (UTC) time whereas trajectory simulation results use time since RV separation. The LOFTID reconstructed mission timeline has RV separation occurring at 11:04:09.241 UTC and Entry Interface occurring at 11:35:03.098 UTC. The reconstructed trajectory simulation result can be found in Table 6.

A. Day-of-Launch Performance

Figure 11 shows the day-of-launch splashdown ellipse with the pre-launch trajectory (PLT) prediction for RV and EDR as well as GPS data. The locator beacon provided GPS data for the LOFTID RV EDL trajectory up until 1.4 km altitude. The black "x" shows the estimated RV splashdown point using the estimated latitude/longitude change over the remaining 1.4 km. Centered about the black "x" are radial distance contours in nautical miles. The green "x" shows the GPS data at splashdown of the EDR. The center of both the RV and EDR PLT ellipses are located within 3 nautical miles of the RV splashdown point, thereby demonstrating the excellent prediction capability of the LOFTID trajectory simulations utilizing GEOS-5 weather forecasts. Figure 11 also shows the GPS movement of the recovery boat as well as the RV and EDR post-splashdown. Prior to launch, the recovery boat moved to within the vicinity of the PLT ellipse centers. Due to a launch delay within the 36 minute launch window and the need to be outside of the Centaur re-entry debris field, the recovery boat moved outside the splashdown ellipse. At a distance of approximately 9 nautical miles, the recovery boat was able to visually observe LOFTID descending by parachute with a stable attitude all the way down to splashdown. Upon visual confirmation of splashdown, the recovery boat moved to rendezvous with LOFTID RV, passing the EDR (with visual confirmation of successful EDR splashdown). The RV was subsequently recovered from the ocean, and the inflatable structure fully retained its structural integrity. After recovery of LOFTID RV, the recovery boat went to recover the EDR. Within the span of a few hours, both the RV and EDR were successfully recovered.

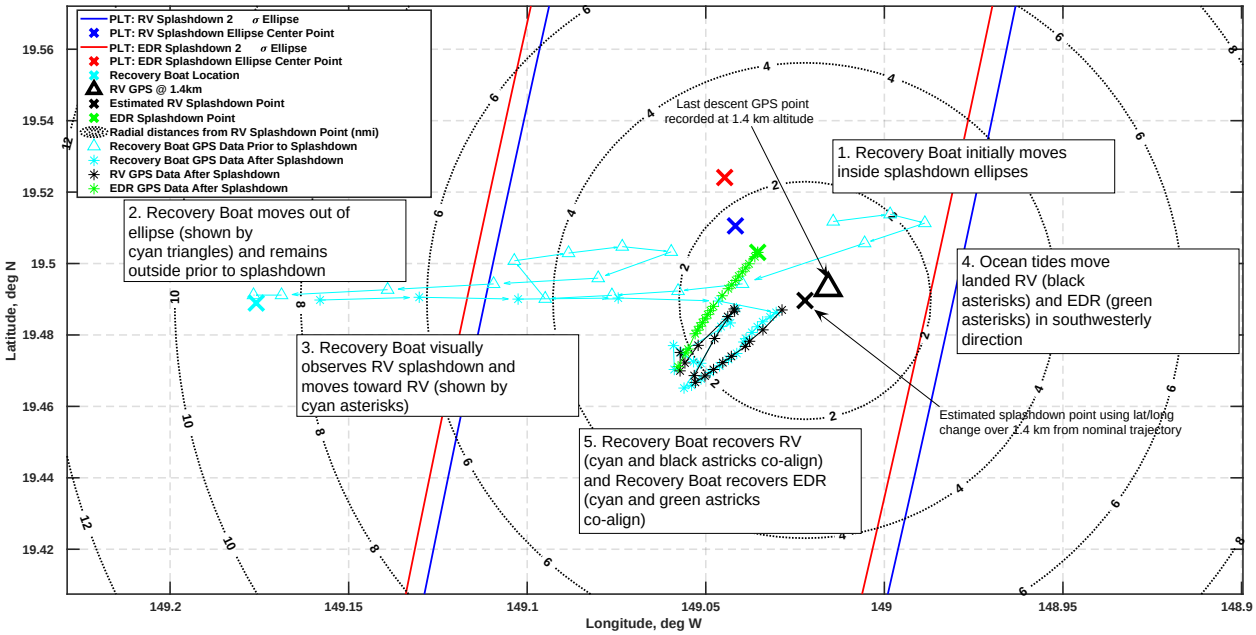

Fig. 11 LOFTID Day-of-Launch Splashdown

During flight, a series of images were obtained at key events during the LOFTID EDL sequence. Figure 12 shows a series of images taken from the Centaur down-look camera that captured LOFTID's secondary payload deployment sequence, including Payload Adapter Separation System (PASS) deployment, RV inflation, and RV separation over the Sinai Peninsula. Figure 13 shows a series of images captured from the various onboard cameras during EDL, including the start of the heat pulse, EDR jettison, and parachute deployment. Figure 14 shows images taken from the recovery boat, including infrared imagery of the RV descending by parachute and the RV post-splashdown.

(a) PASS Deployment (b) RV Inflation (c) RV Separation

Fig. 12 Captured events during LOFTID secondary payload deployment sequence.

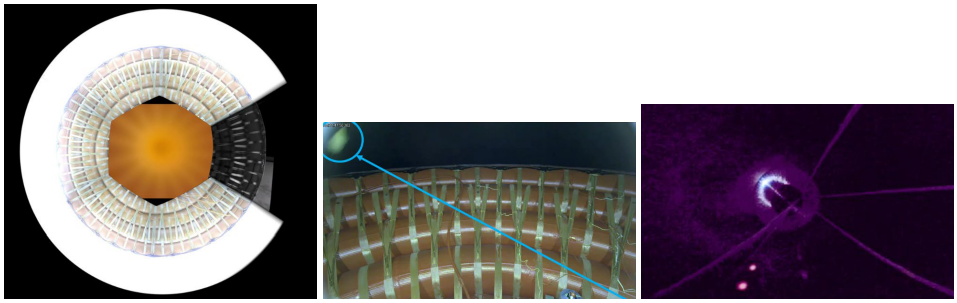

(a) Start of Heat Pulse (b) EDR Jettison (c) Parachute Deployment

Fig. 13 Captured events during LOFTID Entry, Descent, and Landing sequence.

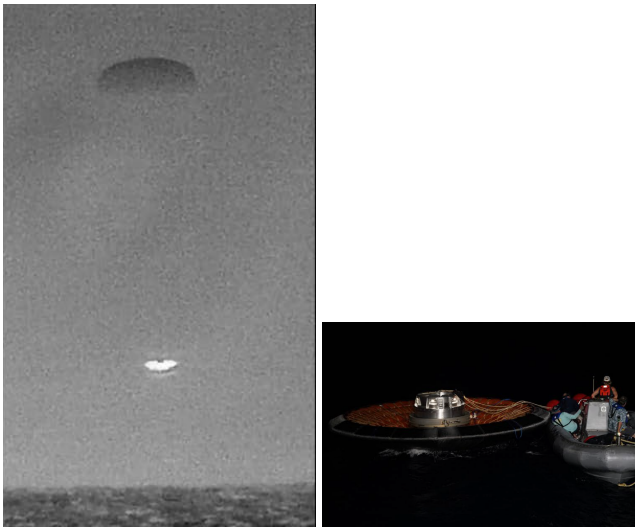

(a) LOFTID Splashdown (b) LOFTID Recovery

Fig. 14 LOFTID splashdown and recovery views from the recovery vessel.

B. Reconstruction Data Sources

The test article was instrumented with a variety of sensors to be used for post-flight evaluation of vehicle performance. Data from one of the key sensors for trajectory reconstruction, the Inertial Measurement Unit (IMU), was not captured in the EDR due to an unforseen malfunction in communication between the analog input module and the network switch [26]. Given the loss of the IMU data, alternate methods for trajectory reconstruction were explored. In particular, attitude reconstruction from on-board video was accomplished, even though the cameras were not calibrated for this purpose or intended to be used for attitude determination. Data from pressure ports in the nose cone, arranged as a Flush Air Data Sensing (FADS) system, were acquired, enabling the reconstruction of the atmospheric-relative trajectory.

1. Atmosphere

The LOFTID ground track spanned a large swath of Earth. After launch from Vandenberg Space Force Base into a near polar orbit, the vehicle circumnavigated the Earth before starting its EDL sequence over Alaska. The vehicle splashed down in the eastern Pacific Ocean to the east of the Island of Hawai'i. Due to the large ground track and remoteness of the landing location, ground-based atmospheric sources for reconstruction, such as weather balloons and meteorological rockets, were not available. Reconstruction of the atmospheric conditions were planned to be based on in-situ measurements from the on-board FADS and IMU instrumentation. Instead, atmospheric reconstruction was conducted using atmosphere model data because the IMU data were lost.

Traditionally, on a mission with FADS and IMU data, such as Mars Science Laboratory and Mars 2020 [27, 28], the atmospheric states are reconstructed from a Kalman filter where atmospheric parameters are estimated. However, due to the failure to save the LOFTID IMU data in the EDR, only FADS data were available. Without an independent estimate of the inertial states from the IMU, it is not possible to separate atmospheric uncertainties from aerodynamic uncertainties in the FADS data. The FADS data have been primarily used for aerodynamic quantities, such as angle of attack. Hence, a separate method was needed for atmospheric reconstruction.

During the design phase for LOFTID, various launch opportunities were evaluated targeting landing areas over unpopulated regions in the Pacific Ocean. Coverage from site-specific atmospheric data, such as range reference atmosphere or radiosonde data, is not available in these areas, so EarthGRAM was used to provide an engineering atmospheric profile. Utilizing EarthGRAM, the atmospheric properties predicted are based on November-average properties with small variations for the time of the day.

During the operations phase of flight, improved atmospheric conditions were needed that pinpointed the landing performance and location to support rapid recovery of the EDR and RV. From previous flight experience [11, 29], EarthGRAM is not well suited in situations where time of the day forecast information is needed.

In order to provide better predictions for operational assets, the LOFTID POST2 simulation incorporated data from the NASA GSFC GMAO tool, which provided temperature, pressure, density, and wind speeds from the surface up to approximately 60 km altitude. The GMAO model is GEOS-5, which provides forecasts of Earth's atmospheric properties in increments of every 3 hr [30]. The forecast is provided in increments of 0.5 deg in latitude and 0.625 deg in longitude, and uncertainties are calculated from a combination of analysis error and forecast error. Since LOFTID was an orbital return mission, the trajectory of the vehicle covered a large area of Earth (see Fig. 15).

Based on analysis during operational support, it was decided to use the vertical profile at 22 deg North and 148.75 deg West from the GEOS-5 analysis for atmospheric parameters. Various latitude and longitudes along the flight path were tested, but the trajectory predictions were not found to be sensitive. Additionally, GMAO had provided forecast uncertainties at this particular point as well, which was useful for modeling in the simulation.

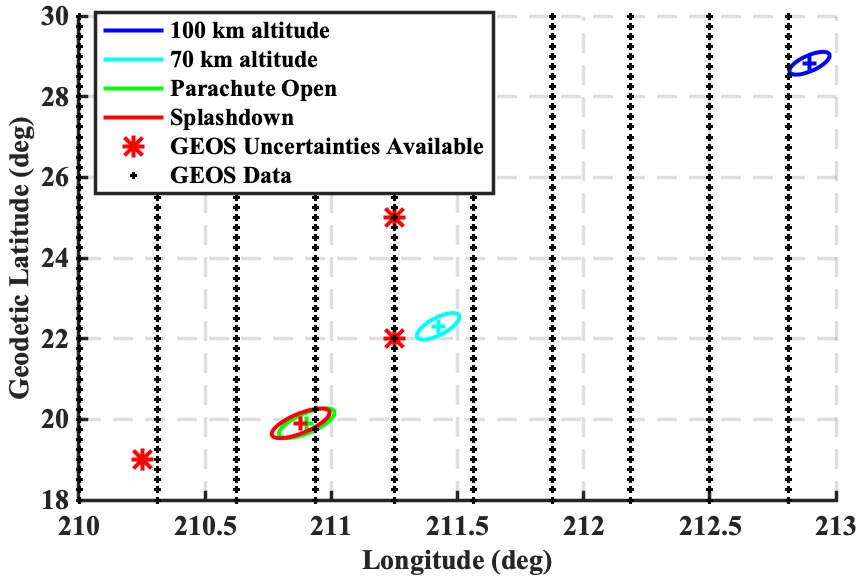

Fig. 15 LOFTID Trajectory at key events and GEOS-5 Forecast Locations

Since LOFTID was an orbital return mission, atmospheric forecast needed for the simulation also included altitudes above the 60 km limit of the GEOS-5 data. Similar to past missions that have used GEOS-5-based forecast data for orbital and sub-orbital flights [29], the 1976 US Standard Atmosphere [31] was used to augment data from GEOS-5. The lapse rate, or the rate of change of temperature with respect to altitude, from the 1976 US Standard Atmosphere was used at corresponding altitudes above 65 km to extend the GEOS-5 temperature prediction. Then, the hydrostatic equation and the perfect gas law were used to calculate the respective pressure and temperature. Wind speeds were assumed to be zero at the atmospheric interface point and linearly varied to the top of the GEOS-5 profiles. The linearly varying assumption is similar to what has been used for other EDL missions [32] to avoid simulating an artificial wind shear by instantaneously making the wind speed zero.

The GEOS-5 reanalysis data from 1200 UTC provided the bulk of the data of the post-flight atmosphere model for LOFTID. However, to extend the atmosphere from approximately 65 km altitude to 125 km altitude, which is the entry interface definition, supplemental data were needed. The authors did not have access to any high quality data set for atmospheric measurements for this area of the Pacific Ocean. Hence, similar to the Adaptable Deployable Entry and Placement Technology Sounding Rocket 1 (ADEPT-SR1) [29] reconstruction, the temperature profile from the 1976 US Standard Atmosphere [31] was used to extend the temperature profile. The post-flight estimates for temperature (Fig. 16), density (Fig. 17), East-West winds (Fig. 18), and North-South winds (Fig. 19) are shown here, along with comparisons to the pre-flight forecast used during operations [13] and the design atmosphere from GRAM. The forecast matches the reanalysis GEOS-5 data, but there are noticeable differences with the GRAM profiles used during the early design phase. One can see deviations between the two models in critical areas such as maximum heating and maximum deceleration, as well as during parachute flight, which occurs below 10 km altitude and affects the landing location.

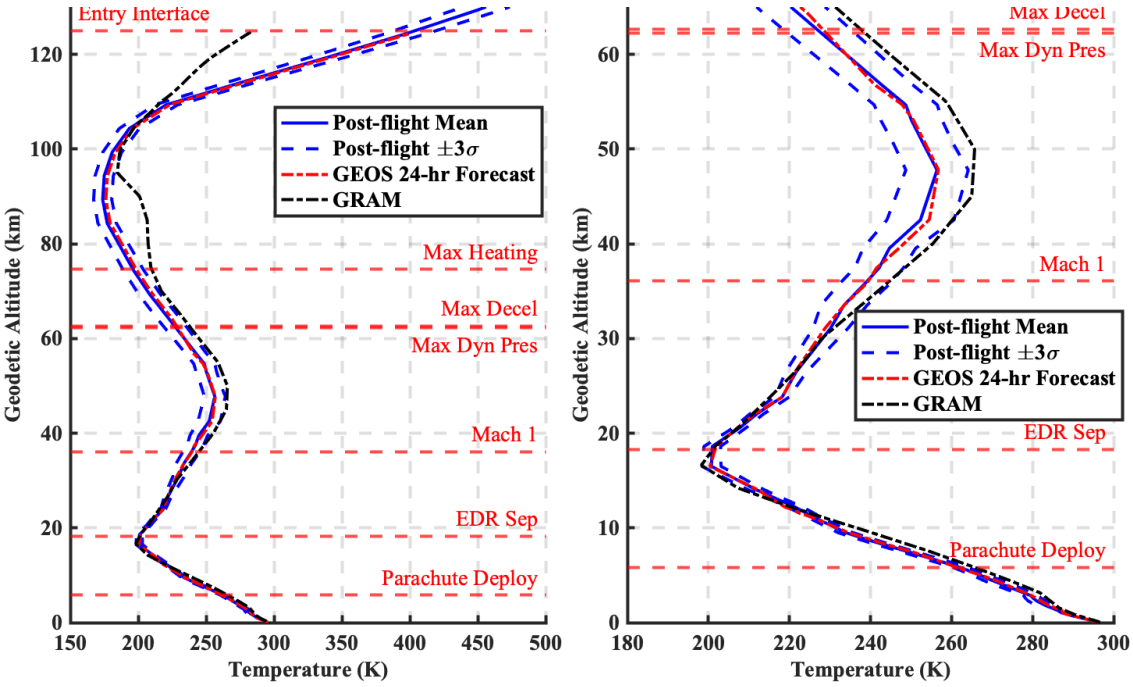

(a) Temperature (b) Temperature (zoomed)

Fig. 16 LOFTID Post-flight Temperature Estimate.

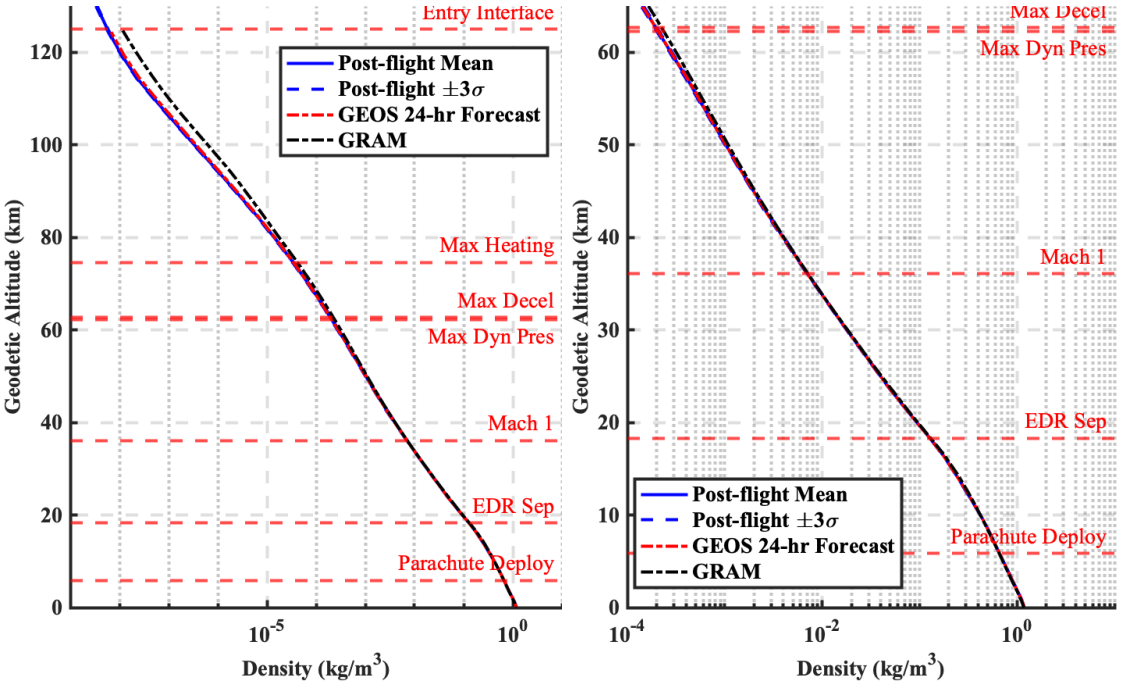

(a) Density (b) Density (zoomed)

Fig. 17 LOFTID Post-flight Density Estimate.

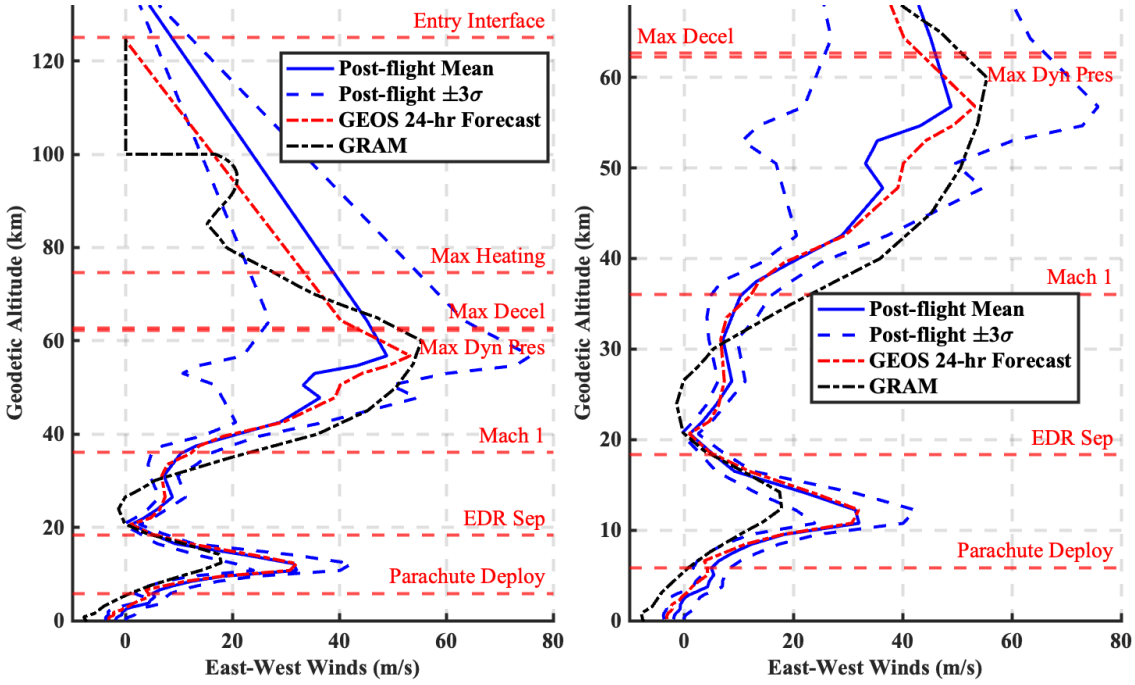

(a) East-West Winds (b) East-West Winds (zoomed)

Fig. 18 LOFTID Post-flight East-West Winds Estimate.

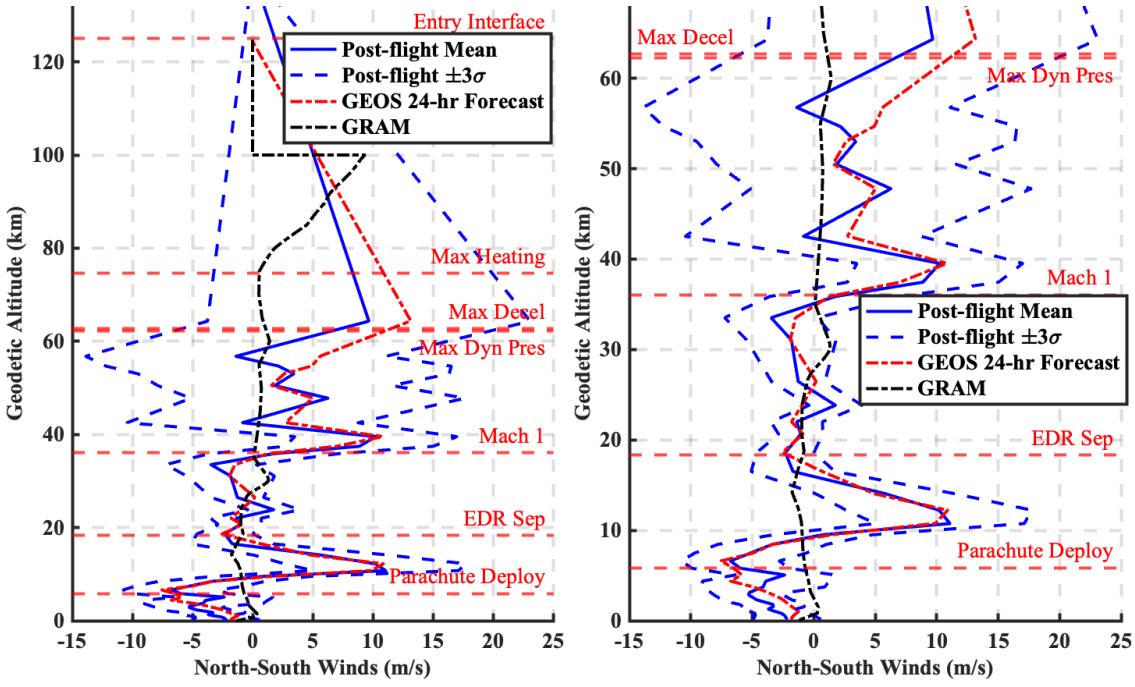

(a) North-South Winds (b) North-South Winds (zoomed)

Fig. 19 LOFTID Post-flight North-South Winds Estimate.

Figure 20 shows a plot comparison of splashdown ellipses for the RV and EDR generated with EarthGRAM and

the 24-hour GEOS-5 forecast from the same initial conditions and vehicle states. The actual landing location, from reconstruction, is also shown in comparison. One can see that the GEOS-5 forecast-based simulation prediction is closer to the actual RV and EDR splashdown points than the EarthGRAM-based prediction. This observation is similar to what was seen in past missions [11, 29]. The ability of forecast model-based predictions to show deviations from original design due to late-breaking atmospheric conditions can allow for improved operational planning of the placement of the recovery boat to facilitate faster recovery. One interesting side effect was that when utilizing the GEOS-5 forecast, there was a reduction in the splashdown ellipse size in both the major and minor axes. This is expected since general models such as EarthGRAM have large uncertainties to account for the large areas of space and time these models need to provide predictions. Other Earth EDL missions can benefit from using forecast-based atmospheric data during operations, as discussed in Ref. [33].

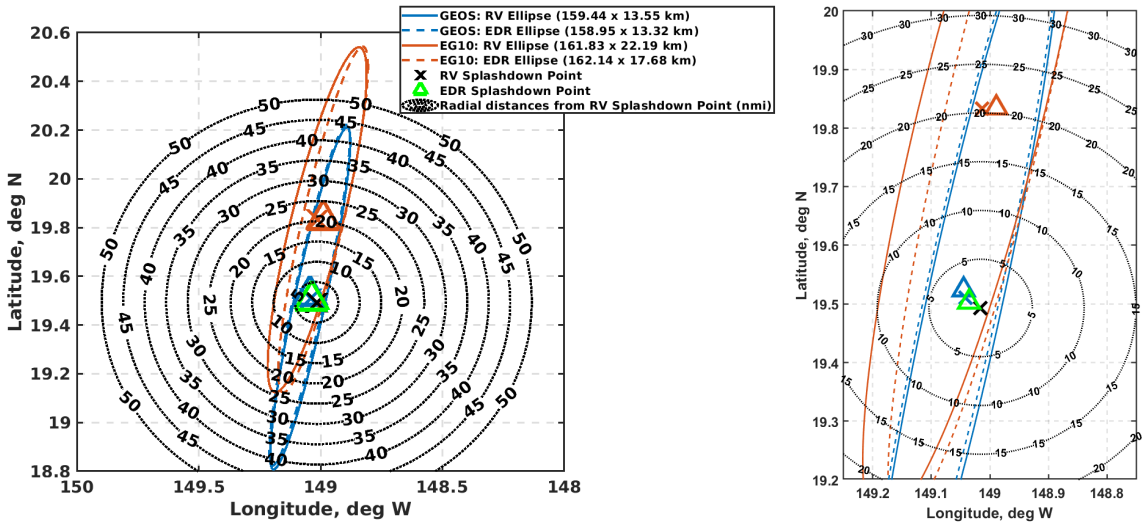

(a) Full (b) Zoomed

Fig. 20 Comparison of GEOS-5 vs EarthGRAM 2010 atmosphere model splashdown ellipses.

2. Video Imaging

LOFTID flew several video cameras attached to the body to record video to be used for visual verification of the heatshield inflation and performance during entry. To this end, a series of six camera pods were placed on the vehicle looking out onto the heat shield to provide full coverage of the entire vehicle, as shown in Fig. 21(a). Note that camera pod 2 was installed on the vehicle but was not functional due to a known hardware issue that could not be fixed prior to flight. A single camera was installed on the body with its field of view pointed aft in order to capture the parachute deployment and inflation. Its installed location is shown in Fig. 21(b). Since the IMU data were lost, an effort was made to use these cameras combined with ephemeris data to reconstruct the attitude and attitude rates of LOFTID where it would be possible to do so in the given video footage.

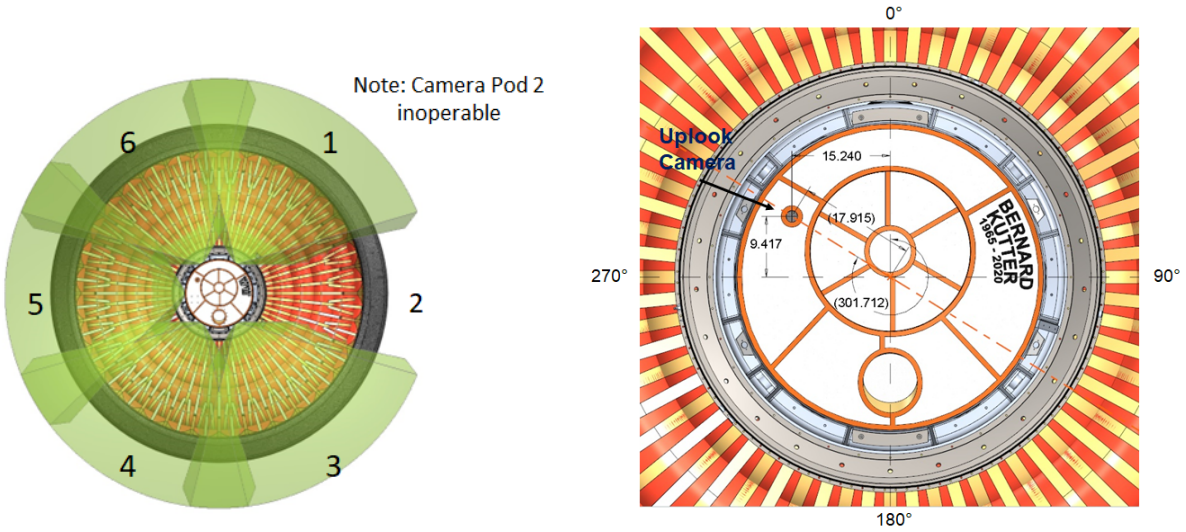

(a) Camera pods.

(b) Uplook camera.

Fig. 21 LOFTID cameras.

The LOFTID camera pod data were processed to extract Earth and Moon unit vectors in the LOFTID body coordinate frame, illustrated in Fig. 22. These two unit vectors meet the minimum set of measurements to determine the vehicle attitude [34]. The video data was processed frame by frame by first masking the LOFTID heatshield and then processing the images to detect the location of the Moon in the camera frame. Next, the limb of the Earth that is contained in the camera field of view was extracted. The position of the Moon within the camera field of view was determined by a simple blob detection algorithm in which the images were filtered by area and circularity thresholding. The position of the center of the Earth in the camera frame was determined by extracting the contour of the visible limb, functioning as a makeshift horizon sensor [35–37], and next generating a sequence of perpendicular bisectors from a set of points along the extracted arc. The Earth center was determined by computing the average intersection point from the family of bisectors.

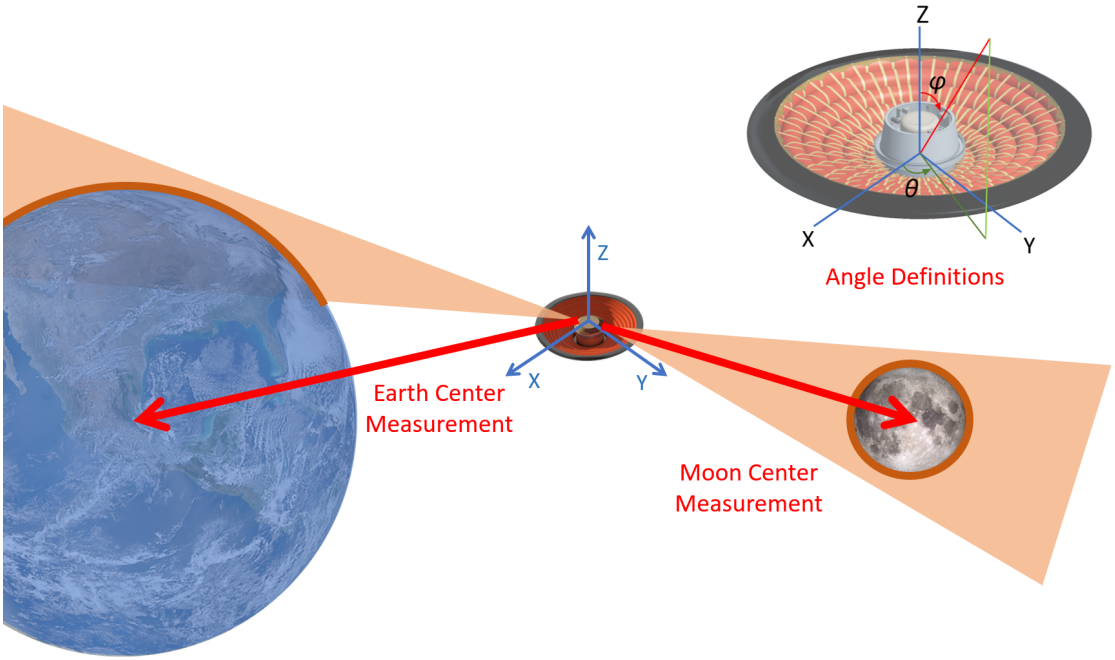

Fig. 22 Earth and Moon vector measurements.

After extracting the centers of the Earth and Moon in the camera frame, the camera pointing vectors relative to the LOFTID vehicle and corrections for optical distortions were used to construct angle measurements of the center of each celestial body relative to the LOFTID vehicle. Three angles are available for determining the attitude of the vehicle: the Moon co-latitude (φ_m) and azimuth (θ_m), and the Earth azimuth (θ_e). The co-latitude and azimuth angles are defined in Fig. 22.

The three angles (φ_m, θ_m, and θ_e) were processed using a Kalman filter formulated to estimate the attitude and angular velocity of the spacecraft [34]. The filter was formulated to estimate the Earth Mean Equator of J2000 (EMEJ2000) [38] quaternion and the body axis angular velocity from the Earth and Moon angle data. The filter process model made use of a constant-angular-velocity model for propagating the attitude between angle measurements. The measurement model was formed by computing unit vectors from the spacecraft to each celestial body in the EMEJ2000 frame, then rotating the vectors into the spacecraft frame to compute the azimuth and co-latitude angles. The position of the Moon in the EMEJ2000 frame required for the measurement model was computed from the Spacecraft, Planet, Instrument, C-Matrix, Events (SPICE) tool [39]. The measurement noise covariance matrix was scheduled as a function of the position of the object within the camera frame to give more uncertainty to objects at the extremities of the camera field of view to account for unmodeled nonlinearities and other camera visual artifacts.

The results of the attitude reconstruction are shown in Fig. 23. The reconstructed EMEJ2000 to body 3-2-1 Euler angles are shown in Fig. 23(a). Note that the Kalman filter was formulated to estimate the quaternion, and the estimated quaternion was converted into the equivalent set of Euler angles for the purpose of showing the attitude history in

Fig. 23(a). As expected, the reconstructed attitudes are consistent with a steady spin of the spacecraft. The reconstructed angular velocity components are shown in Fig. 23(b). The attitude rate reconstruction shows nearly zero rates in the x and y axes and an approximately steady rate in the z axis with a magnitude of approximately 17.7 deg/s, which is within 2% error of the expected nominal spin rate of 18 deg/s [13]. This agreement confirms that the photogrammetry approach applied to LOFTID reconstruction produces a reasonable result.

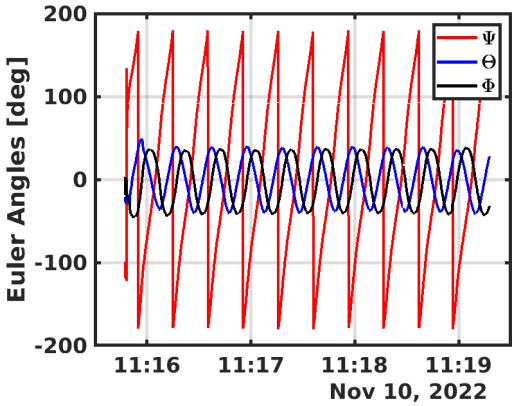

(a) Attitude.

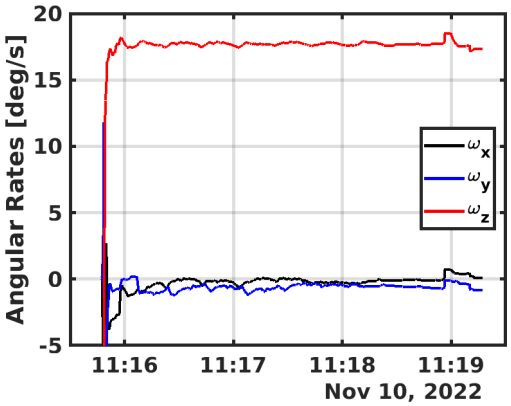

(b) Angular velocity.

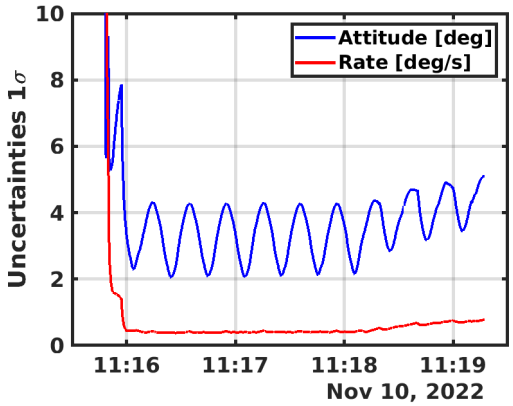

(c) Uncertainties.

Fig. 23 Attitude and angular velocity.

Lastly, the uncertainties of the reconstructed attitude and angular rate are shown in Fig. 23(c). This plot shows the 1σ uncertainty of the total attitude and total rate error. After initial transients, the attitude uncertainty oscillates between approximately 2 to 4 deg and the total rate uncertainty is 0.4 deg/s.

3. Flush Air Data Sensing System

The LOFTID nose cone was instrumented with several sensors, which included five pressure ports installed in a cruciform pattern with one port located at the center of the nose, and two ports in each pitch and yaw plane. The center

port is labeled LPH70, and starting from the positive pitch plane in 90 deg clockwise increments the ports are labeled LPH71 through LPH74. The port layout is shown in Fig. 24(a).

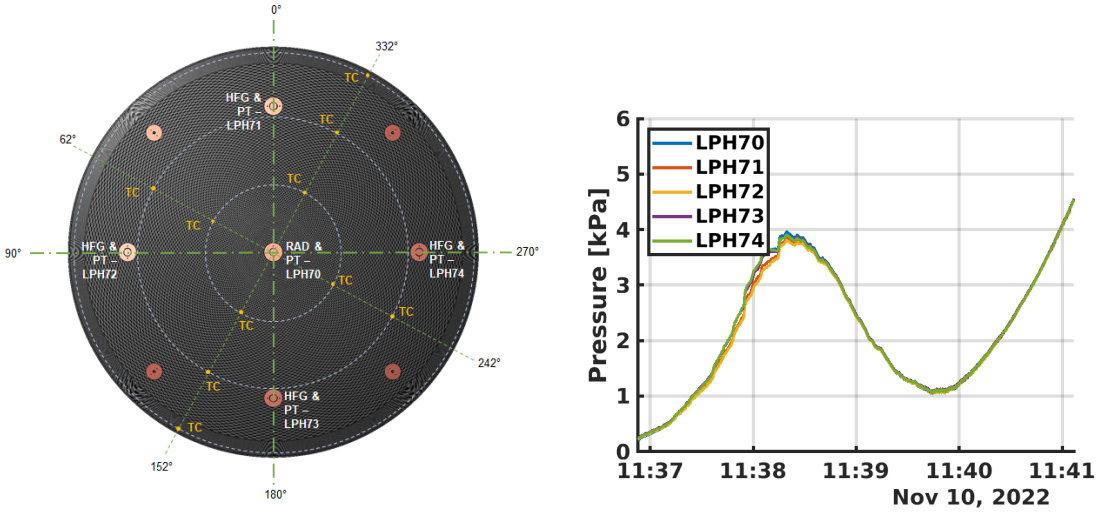

(a) Nose pressure port layout

(b) Measured pressure.

Fig. 24 LOFTID FADS pressures.

The pressures were measured by Druck transducers with a full scale range of 5 V, corresponding to a 10 kPa range. The transducers were calibrated for an operating range of -20 to +80 C in a thermal vacuum chamber. The sensors had a rated accuracy of 0.04% of the full scale range, which was confirmed by ground testing. After flight, the recorded pressures were converted to pressure units by applying the calibration coefficients to the sensor's Volt output and measured operating temperature. The resulting pressure measurements along the atmospheric entry trajectory are shown in Fig. 24(b).

The FADS data were combined with a Newtonian flow pressure model [27, 40] to produce estimates of the atmospheric relative trajectory. A Mach number anchoring technique given in [27] was used to stabilize estimates in high-speed flight conditions. Since no IMU data were available, a trajectory simulation [13] was used to provide the Mach number time history. The resulting estimates of the atmospheric-relative trajectory are shown in Figure 25.

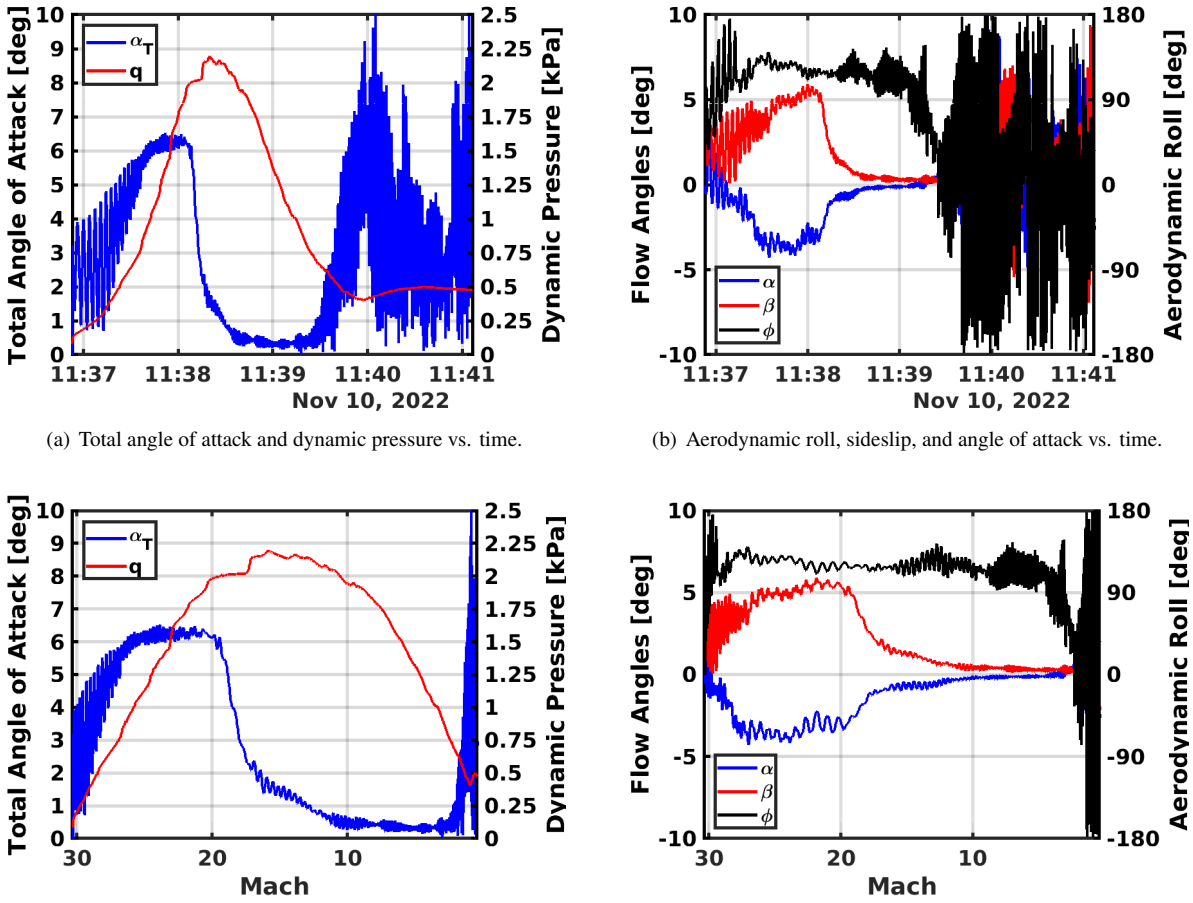

(a) Total angle of attack and dynamic pressure vs. time.

(b) Aerodynamic roll, sideslip, and angle of attack vs. time.

(c) Total angle of attack and dynamic pressure vs. Mach.

(d) Aerodynamic roll, sideslip, and angle of attack vs. Mach.

Fig. 25 FADS reconstructed trajectory.

The peak total angle of attack in the hypersonic flight phase was approximately 6.5 deg. Just prior to peak dynamic pressure, the total angle of attack dropped to approximately 0.5 deg. The hypersonic aerodynamic roll angle was approximately 120 deg, which was consistent with observations from the uplook camera wake video analysis [26]. The peak dynamic pressure was 2.19 kPa. The peak drag force and peak acceleration were 102.8 kN and 9.52 Earth-G, respectively, calculated by assuming nominal aerodynamics database evaluated along the reconstructed trajectory. Note that the slight bump in the dynamic pressure at a Mach number of 18 at 11:38:10 UTC, just prior to the peak pressure could correspond to a density "pot hole," an atmospheric phenomenon that has been observed in Space Shuttle entries [41, 42], IRVE-3 [3], and possibly in the Low-Density Supersonic Decelerator (LDSD) second flight test [43]. Other onboard instruments such as load sensors confirmed this bump in dynamic pressure [26]. The atmospheric density along the trajectory was computed from the reconstructed dynamic pressure and the velocity from the trajectory simulation [13]. Comparisons of the density to the atmospheric data are shown in the following section.

4. Locator Beacon

The locator beacon provided GPS measurements of the spacecraft position during a portion of the atmospheric entry. The beacon was able to acquire satellite observations at an altitude of approximately 18.6 km and below. This altitude range corresponds to the subsonic flight regimes and to the parachute flight phase and so are of limited use for evaluating hypersonic and supersonic flight characteristics of the entry vehicle. The data provide a useful comparison for the terminal descent phase of the trajectory simulation, which is described in Section IV.D.

C. LOFTID As-Flown Aerodynamic Performance

The lack of IMU data severely impaired the reconstruction process. Without the IMU data it was not possible to reconstruct the as-flown trajectory and aerodynamics of the vehicle. Nominal aerodynamics (taken from the ADB) were assumed in order to compute metrics such as loads, which ordinarily would have been directly measured by the IMU. Trajectory information needed in the aerodynamic reconstruction process is provided by POST2 simulation data, as described in Section IV.D.

The reconstructed total angle-of-attack history with the dynamic pressure pulse, shown in Fig. 25 demonstrates success in meeting the LOFTID requirement for RV aerodynamic stability throughout the trajectory, with the total angle of attack remaining below 7 deg prior to peak dynamic pressure and remaining well below the 20 deg requirement afterwards. Prior to peak dynamic pressure, the total angle of attack increases from approximately 1.23 deg at 125 km (atmospheric interface) to a maximum of 6.52 deg, then sharply drops to less than 1 deg with increasing dynamic pressure as the aeroshell shifted position slightly from its zero-g inflation location into its nominal drag location relative to the rigid nose. The RV remained at low total angle of attack past peak dynamic pressure until decelerating to approximately Mach 2 conditions. The peak α_T across the entire reconstructed trajectory was 10.41 deg.

As discussed above, during the hypersonic phase, the RV was unguided but spin-stabilized and began re-entry along a ballistic trajectory with the aeroshell in its zero-g inflation location. Until settled into its nominal drag position on the RV, the aeroshell orientation was sufficiently off-center to trim the RV to a maximum angle of attack of approximately -4.29 deg and sideslip angle of 5.90 deg. As expected, the RV attitude began to increase as the vehicle decelerated through supersonic to subsonic conditions due to the inherent dynamic instability of the shape. The attitude increase can be seen in Fig. 25(a) after 11:39:30 and in Fig, 25(c) as the Mach number decreases into the subsonic regime. The maximum angles of attack and sideslip over the entire reconstructed trajectory were 9.12 deg and 9.39 deg, respectively, well below the 20 deg LOFTID mission requirement for stability. LOFTID was the first flight and opportunity to gather data on the stability and performance of a blunt body aeroshell geometry with no backshell through transonic and subsonic conditions, and on-board video data confirmed no attitude or attitude rate excursions.

D. Best Estimated Trajectory

Typically an IMU forms the most basic set of inputs for purposes of post-flight trajectory reconstruction [44, 45]. The lack of IMU data caused an engineering challenge in trying to ascertain the reconstructed flown trajectory of LOFTID. In lieu of IMU data, POST2 trajectory simulation [13] is utilized wherein available data sources are utilized to reconcile the day-of-flight simulation model inputs. During the reconciliation process, a series of best predicted flown trajectories (BPFT) are generated. Version 0 pertained to the PLT generated prior to LOFTID EDL (see Section II.C). Version 1.0 of the BPFT (BPFTv1) is identical to the PLT with the exception of the utilization of reconciled day-of-flight GEOS-5 atmosphere (see Section IV.B.1). Version 2.0 of the BPFT (BPFTv2) utilizes the orbital parameter message of the the initial position and attitude state at RV separation. This section provides a comparison of the generated BPFT trajectories to available flight data introduced in Section IV.B.

1. GPS Comparison

The location beacon (LB) GPS data is utilized in comparison to the PLT and BPFT versions. Figure 26 provides a trajectory position comparison in latitude/longitude/altitude space. The LB data generally agrees well with the reconciled trajectories, with the best quantitative agreement with BPFTv1. The differences in the trajectories can be attributed to differences in the atmosphere model.

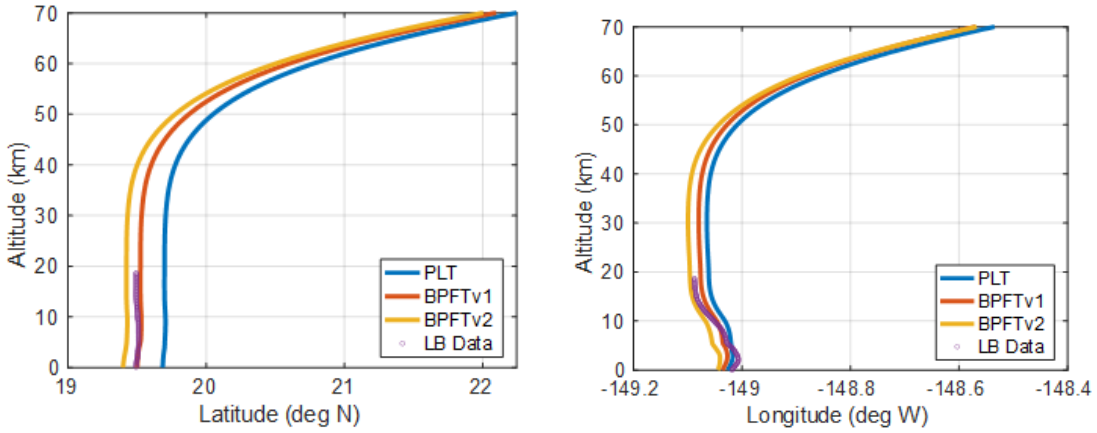

(a) Altitude vs latitude.

(b) Altitude vs longitude.

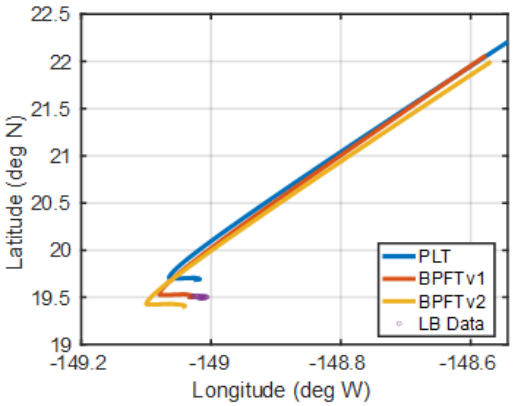

(c) Latitude vs longitude.

Fig. 26 Trajectory comparison with locator beacon position.

Figure 27 provides a trajectory velocity comparison between the LB data and the reconciled trajectories. At a zoomed out view (subplot a), not much difference can be seen between the datasets. Zooming into a region below 10 km altitude (subplot b), the LB data tracks well with BPFTv1 trajectory. Between 7-10 km, the LB data suggests slower deceleration than the trajectories. The two rapid changes in velocity are representative of the LOFTID pilot and main parachute deployments. The LB data agrees to within 10% with the BPFT trajectories between 5 and 7 km indicating pilot chute deployment at 5.8 km and main chute deployment at 5.4 km. The PLT predicted parachute deployments to occur at lower altitudes. Zooming in on the last 1 km shows LB data indicating slightly higher splashdown velocity (7.5 m/s) than the trajectories (all three on top of each other) along with oscillations in velocity. These oscillations are most likely caused by horizontal winds and RV oscillations while descending by parachute prior to splashdown. Overall, LB data agrees well with trajectory estimates and provide quantitative confirmation of successful parachute deployment.

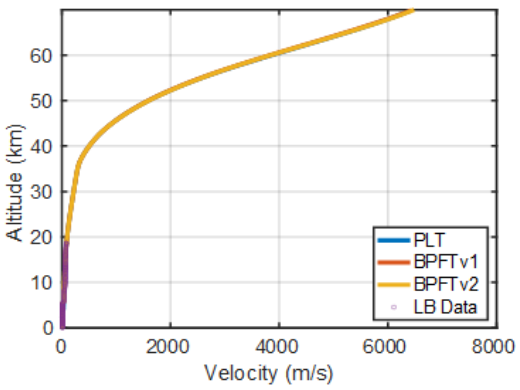

(a) Altitude vs velocity.

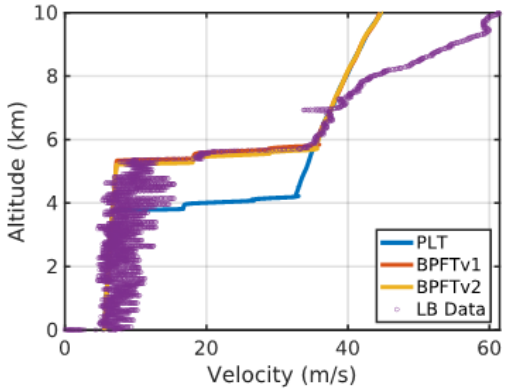

(b) Altitude vs velocity.

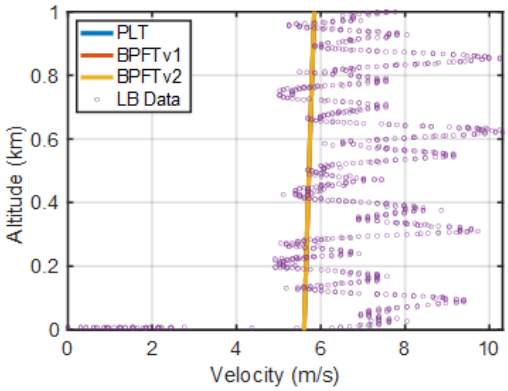

(c) Altitude vs velocity.

Fig. 27 Trajectory comparison with locator beacon velocity.

2. FADS Comparison

The FADS provides engineering measurements of the LOFTID as-flown freestream conditions. The reconstructed dynamic pressure can be utilized in conjunction with the atmosphere-relative velocity to obtain an estimate of the atmospheric density. FADS does not directly measure atmosphere-relative velocity, so the reconstructed trajectory from IMU and atmosphere wind data would be needed. The POST2-generated trajectories are utilized in lieu of IMU data to provide a FADS-estimate of the as-flown density profile. This density profile is utilized in lieu of a reconciled GEOS-5 atmosphere model in BPFTv2 to see what effect it has on the subsequent trajectory output. Figure 28 provides a comparison between the reconstructed FADS data and the POST2 generated trajectories. The FADS density profile generally tracks well with BPFTv1 and BPFTv2 but suggests higher density at altitudes above 60 km (subplot a) (note: FADS and BPFTv2 w/FADS Density will have the same density profile). This slight difference in density leads to faster deceleration when the BPFTv2 trajectory is rerun using the FADS density profile (subplot d). Note that the FADS and BPFTv2 will have the same velocity profile. The combination of higher densities but lower velocities leads

to the BPFTv2 run with the FADS density profile to generate a lower peak dynamic pressure than both the original BPFTv2 trajectory and FADS data (subplot c). The bump in dynamic pressure (65 km, 2000 Pa) measured by FADS corresponding to the suspected density pothole can be incorporated into density to produce the same subsequent effect in the rerun trajectory. This change in result demonstrates the challenge of mixing dependent data sources, such as density dependence on trajectory data, in trying to reconcile differences seen in FADS and BPFT trajectories. Nevertheless, BPFTv1 and BPFTv2 generally agree well with the FADS data for dynamic pressure but do not agree with total angle of attack (subplot b). The FADS data suggests a larger increase in total angle of attack prior to peak dynamic pressure, which is caused by an aeroshell torque not captured in the BPFT trajectories. These rotational dynamics would have been sensed by an IMU.

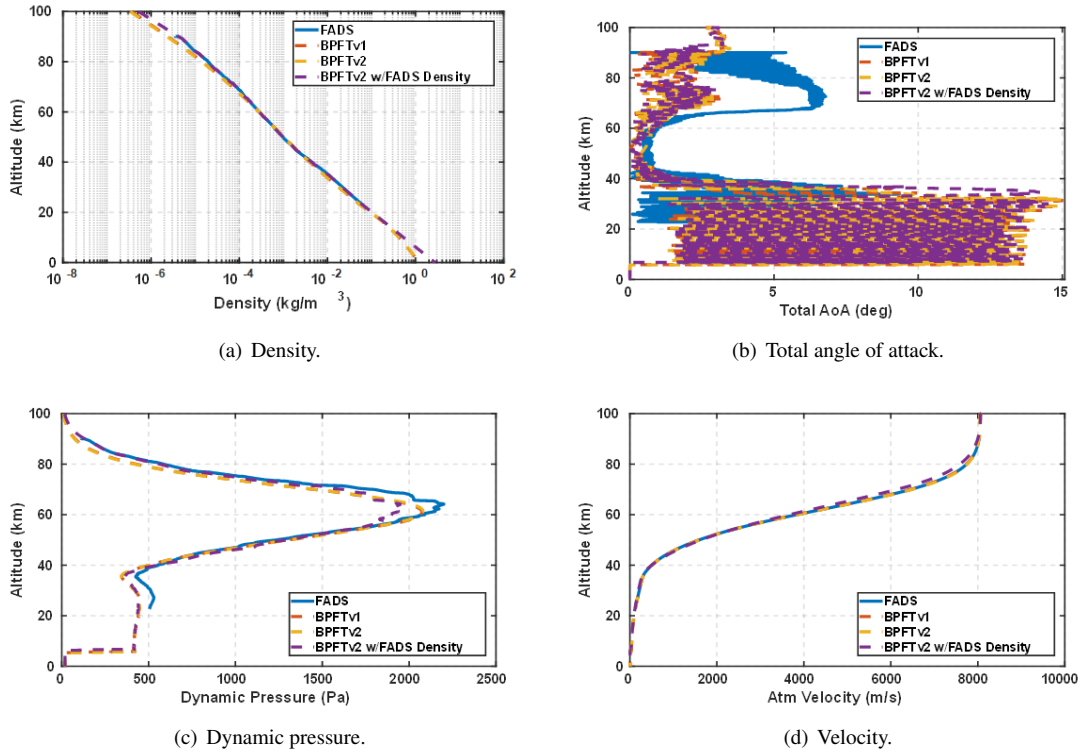

(a) Density.

(b) Total angle of attack.

(c) Dynamic pressure.

(d) Velocity.

Fig. 28 Trajectory comparison.

3. BET at-a-glance

The best estimated trajectory (BET) for LOFTID is generated using BPFTv2. Figure 29 shows a ground track of the trajectory from Centaur separation above the Sinai Peninsula through entry interface and finally splashdown off the coast of Hawaii. Table 6 and Table 7 provides quantitative results for the BET.

After a 30 min spin-stabilized cruise from separation, LOFTID re-entered the atmosphere at a velocity close to 8 km/s. BET estimates a max nose total heat rate close to the desired 40 W/cm^2 value. The percent error of the BET peak

dynamic pressure and peak deceleration with respect to FADS-derived results was 5.07% and 5.63%, respectively.

The EDR jettison was triggered by fixed-timer value of 2260.0 s after RV separation. The timed trigger was set based on the longest possible time of flight within the launch window. The BET estimates the jettison event to have occurred at 18.17 km altitude, Mach 0.29. LOFTID launched in the back third of the launch window, resulting in a shorter time of flight, and subsequently, the EDR deployed significantly later than the Mach 0.7 target condition.

The pilot chute was triggered by fixed-timer value of 2509 s after RV separation, which was based on longest possible time of flight within launch window. Similar to the EDR jettison, the shorter time-of-flight caused pilot chute followed by the main chute to deploy later than desired. The BET estimates the pilot chute deployed at Mach 0.11, 5.72 km altitude, 2.09 deg total angle of attack, and the main parachute deployment at Mach 0.09, 5.59 km altitude.

The BET estimates the RV splashdown occured 56 min after separation at a point 5.5346 nmi from the GPS-recorded splashdown point.

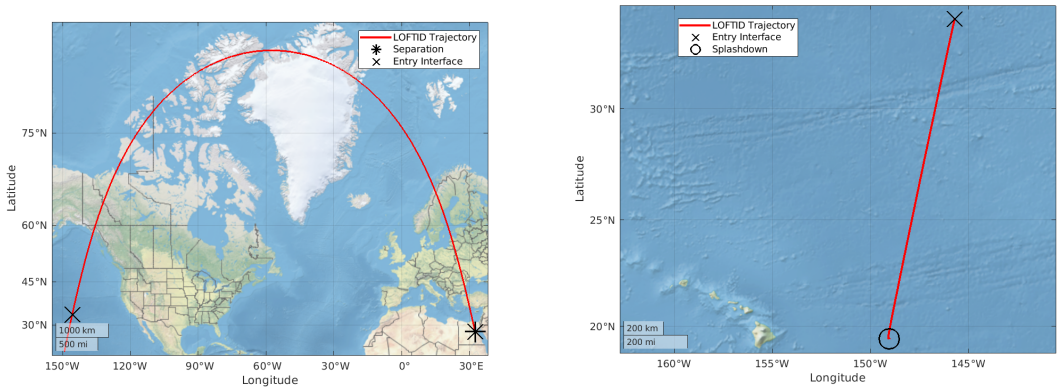

(a) Separation to splashdown.

(b) Entry interface to splashdown.

Fig. 29 LOFTID best estimated trajectory.

Table 6 LOFTID best estimated trajectory data.

Parameter	Value
RV Separation	
ECEF X (km)	5268.7913
ECEF Y (km)	3349.8203
ECEF Z (km)	3224.9374
ECEF Vx (km/s)	-1.9751
ECEF Vy (km/s)	-3.1591
ECEF Vz (km/s)	6.4241
Pitch Angle (deg)	-60.4903
Yaw Angle (deg)	164.8808
Roll Angle (deg)	-143.8753
Pitch Rate (deg/s)	0.0428
Yaw Rate (deg/s)	-0.0628
Roll Rate (deg/s)	-18.0230
Entry Interface	
Time Since Separation (sec)	1853.8567
Inertial Velocity (km/s)	7.9466
Inertial Flight Path Angle (deg)	-2.2933
Geodetic Latitude (deg)	33.8818
Longitude (deg)	214.2874
Azimuth (deg)	189.6399
Geodetic Altitude (km)	125.0000
Total Angle of Attack (deg)	1.2258
Pitch Rate (deg/s)	-0.1197
Yaw Rate (deg/s)	-0.1290
Roll Rate (deg/s)	-18.0223
EDL Metrics	
Peak Deceleration (Earth G)	8.9842
Peak Dynamic Pressure (Pa)	2079.7396
Total Angle of Attack @ Max Nose Heating (deg)	0.1294
Max Nose Heat Rate (W/cm^2)	39.7720
Max Nose Heat Load (kJ/cm^2)	3.4516
Time Since Entry @ Peak Nose Heating (sec)	161.2433
Time Since Entry @ Peak Deceleration (sec)	201.3633
Time Since Entry @ Peak Dynamic Pressure (sec)	202.4633
Geodetic Altitude @ Peak Nose Heating (km)	73.8274
Geodetic Altitude @ Peak Deceleration (km)	61.7327
Geodetic Altitude @ Peak Dynamic Pressure (km)	61.3921
Mach @ Peak Nose Heating	25.3898
Mach @ Peak Deceleration	14.2717
Mach @ Peak Dynamic Pressure	13.9253

*Table continued on next page

Table 7 Continuation of Table 6

Parameter	Value
EDR Jettison	
Time Since Separation (sec)	2260.0000
Geodetic Altitude (km)	18.1705
Total Angle of Attack (deg)	4.3587
Mach Number	0.2878
Time to EDR splashdown	330.7363
Pilot Chute Trigger	
Time Since Separation (sec)	2509.0000
Geodetic Altitude (km)	5.7164
Total Angle of Attack (deg)	2.0889
Mach Number	0.1084
Velocity (m/s)	35.2081
Time to Main Chute (sec)	3.8720
Main Chute Begin	
Geodetic Altitude (km)	5.5917
Mach Number	0.0881
Velocity (m/s)	28.6530
Time to RV splashdown (sec)	843.5669
Splashdown	
Time Since Separation (sec)	3356.4389
Horizontal Velocity (m/s)	2.8577
Vertical Velocity (m/s)	5.6033
Off-Vertical Angle (deg)	0.0039
Geodetic Latitude (deg)	19.3982
Longitude (deg)	210.9555
Distance from GPS Splashdown Point (nmi)	5.5346

V. Conclusions

The LOFTID mission successfully demonstrated the deployment and entry performance of a 6 m diameter Hypersonic Inflatable Aerodynamic Decelerator from low-Earth orbit on November 10, 2022. Both the re-entry vehicle and ejectable data module were successfully recovered from the Pacific Ocean, with LOFTID satisfying requirements for decelerator performance and stable flight from orbital entry conditions through parachute deployment and splashdown. LOFTID demonstrated inflatable aeroshell technology at scale and conditions relevant to multiple EDL applications, including Earth and Mars, further advancing the capability for low-mass, high performance decelerator systems.

The reconciled trajectories generated by the EDL simulation agree well with available flight data. The lack of IMU data makes it difficult to generate a pure trajectory reconstruction of the as-flown LOFTID trajectory with independent data sources. Though the critical IMU data were not captured, other data sources were used to reconstruct the flight

performance of the vehicle during atmospheric entry.

From the LOFTID mission, a few lessons learned can be applied for future Earth tests. The utilization of forecast atmosphere models played a critical role in improving day-of-flight trajectory predictions to faciliate rapid recovery of LOFTID RV and EDR. Future missions should employ utilizing forecasts models, such as GEOS-5, to help better improve their flight operations processes. Furthermore, future missions should incorporate mitigation strategies to avoid critical flight data loss, such as IMU. Redundant systems and/or thorough launch vehicle integration testing should be conducted. Despite the loss of IMU data for LOFTID, the mission was able to utilize nontraditional measurements systems, such as onboard video cameras, to obtain both qualitative and quantitative flight data.

Appendix

Acronyms

ADB Aerodynamics Database

$ADEPT-SR1$ Adaptable Deployable Entry and Placement Technology Sounding Rocket 1

BET Best Estimated Trajectory

$BPFT$ Best Predicted Flown Trajectory

CFD Computational Fluid Dynamics

DAC DSMC Analysis Code

DOF Degrees-of-Freedom

$DSMC$ Direct Simulation Monte Carlo

EDL Entry Descent and Landing

EDR Ejectable Data Recorder

$EMEJ2000$ Earth Mean Equator J2000

$FADS$ Flush Air Data Sensing

$FUN3D$ Fully Unstructured Navier-Stokes 3-Dimensional

$GEOS-5$ Goddard Earth Observing System Version 5

$GMAO$ Global Modeling and Assimilation Office

GPS Global Positioning System

$GRAM$ Global Reference Atmospheric Model

$GSFC$ Goddard Space Flight Center

$HIAD$ Hypersonic Inflatable Aerodynamic Decelerator

IMU Inertial Measurement Unit

$IRVE$ Inflatable Reentry Vehicle Experiment

$JPSS-2$ Joint Polar Satellite System 2

KSC Kennedy Space Center

$LaRC$ Langley Research Center

$LAURA$ Langley Aerothermodynamic Upward Relaxation Algorithm

LB Locator Beacon

$LDSD$ Low-Density Supersonic Decelerator

$LOFTID$ Low-Earth Orbit Flight Test of an Inflatable Decelerator

MAP Multiphysics Algorithm with Particles

$MSFC$ Marshall Space Flight Center

$NewSTEP$ New Statistical Trajectory Estimation Program

$NOAA$ National Oceanic and Atmospheric Administration

OPM Orbital Parameter Update

$PASS$ Payload Adapter Separation System

PLT Post-Launch Trajectory

$POST2$ Program to Optimize Simulated Trajectories II

PT Pre-Launch Trajectory

RV Re-entry Vehicle

ULA United Launch Alliance

UTC Coordinated Universal Time

Acknowledgments

The authors would like to acknowledge the support from the NASA Space Technology Mission Directorate's Technology Demonstration Mission Program and NASA's partnership with United Launch Alliance on this mission. The authors would like to thank the entire LOFTID team for a successful launch and EDL mission.

References

[1] Cianciolo, A. D., and Polsgrove, T., "Human Mars Entry, Descent, and Landing Architecture Study: Phase 2 Summary," AIAA Paper 2018-5190, September 2018. https://doi.org/10.2514/6.2018-5190.

[2] Hughes, S. J., Dillman, R. A., Starr, B. R., Stephan, R. A., Lindell, M. C., Player, C. J., and Cheatwood, F. M., "Inflatable Reentry Vehicle Experiment (IRVE) Design Overview," AIAA Paper 2005–1636, May 2005. https://doi.org/10.2514/6.2005-1636.

[3] Olds, A. D., Beck, R. E., Bose, D. M., White, J. P., Edquist, K. T., Hollis, B. R., Lindell, M. C., Cheatwood, F. M., Gsell, V. T.,

and Bowden, E. L., "IRVE-3 Post-Flight Reconstruction," AIAA Paper 2013–1390, March 2013. https://doi.org/10.2514/6.2013-1390.

[4] Williams, R. A., Lugo, R. A., Marsh, S. M., Hoffman, J. A., Shidner, J. D., and Aguirre, J. T., "Enabling Thread Safety and Parallelism in the Program to Optimize Simulated Trajectories II," AIAA Paper 2018-5190, January 2023. https://doi.org/10.2514/6.2023-0148.

[5] Williams, R. A., Lugo, R. A., and Hoffman, J. A., "Design of an Application Programming Interface for the Program to Optimize Simulated Trajectories II," AIAA Paper 2024-0161, January 2024. https://doi.org/10.2514/6.2024-0161.

[6] Bodkin, R. J., Akamine, R. L., Blakeley, H. S., Brewster, P. F., Cheatwood, F. M., Clark, T. O., Dillman, R. A., DiNonno, J. C., Emmett, A. L., Hancock, S. M., Hughes, S. J., Mosher, R. N., and Saulman, B. M., "The Design of the Low-Earth Orbit Flight Test of an Inflatable Decelerator (LOFTID) Reentry Vehicle (RV)," AIAA Paper 2024–1310, January 2024. https://doi.org/10.2514/6.2024-1310.

[7] Hollis, B. R., Wise, A. J., Liechty, D. S., Korzun, A. M., Thompson, K. B., Rodrigues, N. S., and Rieken, E., "Aerothermodynamics Analyses for the LOFTID Technology Demonstration Mission," AIAA Paper 2024–1498, January 2024. https://doi.org/10.2514/6.2024-1498.

[8] White, P. W., and Hoffman, J., "Earth Global Reference Atmospheric Model (Earth-GRAM): User Guide," NASA TM-2021-0022157, September 2021.

[9] Molod, A., Takacs, L., Suarez, M., Bacmeister, J., Song, I., and Eichmann, A., "The GEOS-5 Atmospheric General Circulation Model: Mean Climate and Development from MERRA to Fortuna," NASA TM- 104606-VOL-28, April 2012.

[10] Rienecker, M. M., Suarez, M. J., Todling, R., Bacmeister, J., Takacs, L., Liu, H. C., Gu, W., Sienkiewicz, M., Koster, R., Gelaro, R., Stajner, I., , and Nielsen, J., "The GEOS-5 Data Assimilation System - Documentation of Versions 5.0.1, 5.1.0, and 5.2.0," NASA TM- 2008-104606-VOL-27, December 2008.

[11] Dutta, S., Karlgaard, C., Tynis, J., O'Farrell, C., Sonneveldt, B., Queen, E., Bowes, A., Leyleck, E., and Ivanov, M., "Advanced Supersonic Parachute Inflation Research Experiment Preflight Trajectory Modeling and Postflight Reconstruction," *Journal of Spacecraft and Rockets*, Vol. 57, No. 6, 2020, pp. 1387–1407. https://doi.org/10.2514/1.A34706.

[12] Dutta, S., Way, D., Zumwalt, C., and Blette, D., "Postflight Assessment of Mars 2020 Entry, Descent, and Landing Simulation," *Journal of Spacecraft and Rockets*, Vol. 61, No. 3, 2024, pp. 847–857. https://doi.org/10.2514/1.A35771.

[13] Deshmukh, R. G., Dutta, S., Bowes, A., and DiNonno, J. C., "Flight Mechanics Analysis of Low-Earth Orbit Flight Test of an Inflatable Decelerator," AIAA Paper 2024–1501, January 2024. https://doi.org/10.2514/6.2024-1501.

[14] Moss, J. N., Glass, C. E., Hollis, B. R., and Norman, J. W. V., "Low-Density Aerodynamics for the Inflatable Reentry Vehicle Experiment," *Journal of Spacecraft and Rockets*, Vol. 43, No. 6, 2006, pp. 1191–1201. https://doi.org/10.2514/1.22707.

[15] Schoenenberger, M., Cheatwood, F. M., and Desai, P. N., "Static Aerodynamics of the Mars Exploration Rover Entry Capsule," AIAA Paper 2005–0056, January 2005. https://doi.org/10.2514/6.2005-56.

[16] Edquist, K. T., Desai, P. N., and Schoenenberger, M., "Aerodynamics for Mars Phoenix Entry Capsule," *Journal of Spacecraft and Rockets*, Vol. 48, No. 5, 2011, pp. 713–726. https://doi.org/10.2514/1.46219.

[17] Schoenenberger, M., Norman, J. W. V., Karlgaard, C. D., Kutty, P., and Way, D. W., "Assessment of the Reconstructed Aerodynamics of the Mars Science Laboratory Entry Vehicle," *Journal of Spacecraft and Rockets*, Vol. 51, No. 4, 2014, pp. 1076–1093. https://doi.org/10.2514/1.A32794.

[18] Lebeau, G. J., and Lumkin, F. E., "Application Highlights of the DSMC Analysis Code (DAC) Software for Simulating Rarefied Flows," *Computer Methods in Applied Mechanics and Engineering*, Vol. 191, No. 6-7, 2001, pp. 595–609. https://doi.org/10.1016/S0045-7825(01)00304-8.

[19] Liechty, D. S., "Object-Oriented/Data-Oriented Design of a Direct Simulation Monte Carlo Algorithm," AIAA Paper 2014–2456, June 2014. https://doi.org/10.2514/6.2014-2546.

[20] Mazaheri, A., Gnoffo, P. A., Johnson, C. O., and Kleb, W. L., "LAURA User's Manual: 5.5-65135," NASA TM- 2013-217800, February 2013.

[21] Biedron, R. T., Carlson, J., Derlaga, J. M., Gnoffo, P. A., and et al., "FUN3D Manual: 13.5," NASA TM- 2019-220271, April 2019.

[22] Gnoffo, P. A., "An Upwind-Biased, Point-Implicit Algorithm for Viscous, Compressible Perfect-Gas Flows," NASA TP- 2953, February 1990.

[23] Korzun, A. M., Maddock, R. W., Schoenenberger, M., Edquist, K. T., Zumwalt, C. H., and Karlgaard, C. D., "Aerodynamic Performance of the InSight Mars Lander," *Journal of Spacecraft and Rockets*, Vol. 58, No. 5, 2021, pp. 1522–1529. https://doi.org/10.2514/1.A35085.

[24] Kazemba, C. D., Braun, R. D., Schoenenberger, M., and Clark, I. G., "Dynamic Stability Analysis of Blunt-Body Entry Vehicles Using Time-Lagged Aftbody Pitching Moments," *Journal of Spacecraft and Rockets*, Vol. 52, No. 2, 2015, pp. 393–403. https://doi.org/10.2514/1.A32894.

[25] Wilmoth, R. G., Blanchard, R. C., and Moss, J. N., "Rarefied Bridging of Blunt Body Aerodynamics," *Proceedings of the 21st International Symposium on Rarefied Gas Dynamics*, 1998, pp. 1–8.

[26] Swanson, G. T., Kazemba, C. D., Miller, R. A., Alpert, H. S., Williams, J. D., Hughes, S. J., and Cheatwood, F. M., "Overview and Performance of the LOFTID Instrumentation Suite," AIAA Paper 2024–1712, January 2024. https://doi.org/10.2514/6.2024-1712.

[27] Karlgaard, C., Kutty, P., Schoenenberger, M., Munk, M., Little, A., Kuhl, C., and Shidner, J., "Mars Science Laboratory Entry Atmospheric Data System Trajectory and Atmosphere Reconstruction," *Journal of Spacecraft and Rockets*, Vol. 51, No. 4, 2014, pp. 1029–1047. https://doi.org/10.2514/1.A32770.

[28] Karlgaard, C., Schoenenberger, M., Dutta, S., and Way, D., "Mars Entry, Descent, and Landing Instrumentation 2 Trajectory and Atmosphere Reconstruction," *Journal of Spacecraft and Rockets*, Vol. 60, No. 1, 2023, pp. 199–214. https://doi.org/10.2514/1.A35440.

[29] Dutta, S., Karlgaard, C., Korzun, A., Green, J., Tynis, J., Williams, J., Yount, B., Cassell, A., and Wercinski, P., "Adaptable Deployable Entry and Placement Technology Sounding Rocket One Modeling and Reconstruction," *Journal of Spacecraft and Rockets*, Vol. 59, No. 1, 2021, pp. 236–259. https://doi.org/10.2514/1.A35090.

[30] Gelaro, R., McCarty, W., Suarez, M. J., Todling, R., Molod, A., Takacs, L., Randles, C. A., Darmenov, A., Bosilovich, M. G., Reichle, R., Wargan, K., Coy, L., Cullather, R., Draper, C., Akella, S., Buchard, V., Conaty, A., da Silva, A. M., Gu, W., Kim, G.-K., Koster, R., Lucchesi, R., Merkova, D., Nielsen, J. E., Partyka, G., Pawson, S., Putman, W., Rienecker, M., Schubert, S. D., Sienkiewicz, M., and Zhao, B., "The Modern-Era Retrospective Analysis for Research and Applications, Version 2 (MERRA-2)," *Journal of Climate*, Vol. 30, No. 14, 2017, pp. 5419–5454. https://doi.org/10.1175/JCLI-D-16-0758.1.

[31] "U.S. Standard Atmosphere, 1976," NASA TM- X-74335, NOAA-S/T-76-1562, October 1976.

[32] Dutta, S., Karlgaard, C., Kass, D., Mischna, M., and Villar III, G., "Postflight Analysis of Atmospheric Properties from Mars 2020 Entry, Descent, and Landing," *Journal of Spacecraft and Rockets*, Vol. 60, No. 3, 2023, pp. 1022–1033. https://doi.org/10.2514/1.A35561.

[33] Dutta, S., "Use of Forecast Atmospheric Data for Earth Entry, Descent, and Landing Missions," *Journal of Spacecraft and Rockets*, Vol. Articles in Advance, 2024. https://doi.org/10.2514/1.A36119.

[34] Markley, F., and Crassidis, J., *Fundamentals of Spacecraft Attitude Determination and Control*, 1st ed., Springer, New York, 2014, Chaps. 5, 6. https://doi.org/10.1007/978-1-4939-0802-8.

[35] Ouyang, G., Dong, X., and Li, X., "Micro-Satellite Attitude Determination with Only A Single Horizon Sensor," *International Conference on Mechanical, Manufacturing, Modeling and Mechatronics,* Kuala Lumpur, Malaysia, 2016. https://doi.org/10.1051/matecconf/20165103008.

[36] Saadat, A., "Attitude Determination with Self-Inspection Cameras Repurposed as Earth Horizon Sensors," Paper SSC22-VII-03*, International Conference on Mechanical,36th Annual Small Satellite Conference,* Logan, UT, 2022.

[37] Braun, B., and Barf, J., "Image Processing Based Horizon Sensor for Estimating the Orientation of Sounding Rockets, Launch Vehicles and Spacecraft," *CEAS Space Journal*, Vol. 15, No. 1, 2023, pp. 509–533. https://doi.org/10.1007/s12567-022-00461-0.

[38] Tapley, B., Schutz, B., and Born, G., *Statistical Orbit Determination*, Elsevier, Amsterdam, 2004, Chap. 2. https://doi.org/10.1016/B978-0-12-683630-1.X5019-X.

[39] Acton, C., Bachman, N., Semenov, B., and Wright, E., "A Look Towards the Future in the Handling of Space Science Mission Geometry," *Planetary and Space Science*, Vol. 150, No. 1, 2018, pp. 9–12. https://doi.org/10.1016/j.pss.2017.02.013.

[40] Pruett, C., Wolf, H., Heck, M., and Siemers, P., "Innovative Air Data System for the Space Shuttle Orbiter," *Journal of Spacecraft and Rockets*, Vol. 20, No. 1, 1983, pp. 61–69. https://doi.org/10.2514/3.28357.

[41] Findlay, J., Kelly, G., and Troutman, P., "FINAL REPORT - Shuttle Derived Atmospheric Density Model Part 1," NASA CR-171824, December 1984.

[42] Findlay, J., Kelly, G., and Troutman, P., "FINAL REPORT - Shuttle Derived Atmospheric Density Model Part 2," NASA CR-171824, December 1984.

[43] Karlgaard, C., Kutty, P., O'Farrell, C., Blood, E., Ginn, J., and Schoenenberger, M., "Reconstruction of Atmosphere, Trajectory, and Aerodynamics for the Low-Density Supersonic Decelerator Project," *Journal of Spacecraft and Rockets*, Vol. 56, No. 1, 2019, pp. 221–240. https://doi.org/10.2514/1.A34223.

[44] Karlgaard, C., Tartabini, P., Blanchard, R., Kirsch, M., and Toniolo, M., "Hyper-X Post-Flight Trajectory Reconstruction," *Journal of Spacecraft and Rockets*, Vol. 43, No. 1, 2006, pp. 105–115. https://doi.org/10.2514/1.12733.

[45] Karlgaard, C., Beck, R., Derry, S., Brandon, J., Starr, B., Tartabini, P., and Olds, A., "Ares I-X Trajectory Reconstruction: Methodology and Results," *Journal of Spacecraft and Rockets*, Vol. 50, No. 3, 2013, pp. 641–661. https://doi.org/10.2514/1.A32345.